Special Section:
Reactive Transport Modeling

S.A. Bea*
S.A. Wilson
K.U. Mayer
G.M. Dipple
I.M. Power
P. Gamazo

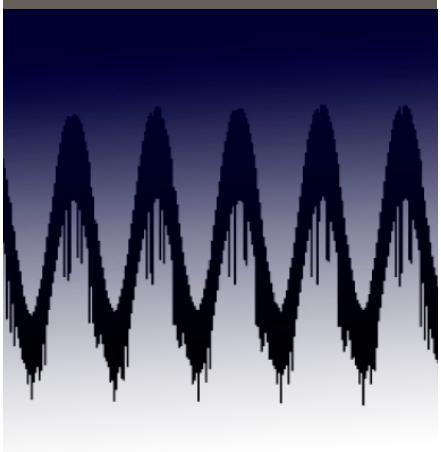

Natural carbon dioxide sequestration is assessed with a process-based reactive transport model for a mine site near Mount Keith, Australia. The simulations demonstrate that atmospheric carbon dioxide is trapped in the ultramafic mine tailings due to carbonation reactions involving the weathering of serpentine and brucite, resulting in the formation of hydromagnesite.

S.A. Bea and K.U. Mayer, Dep. of Earth and Ocean Sciences, Univ. of British Columbia, 6339 Stores Rd., V6T 1Z4, Vancouver, BC, Canada; S.A. Wilson, G.M. Dipple, and I.M. Power, Mineral Deposit Research Unit, Dep. of Earth and Ocean Sciences, Univ. of British Columbia, 6339 Stores Rd., V6T 1Z4, Vancouver, BC, Canada; S.A. Wilson, currently at School of Geosciences, Monash Univ., Clayton, VIC 3800, Australia; P. Gamazo, Water Dep., North Headquarters, Univ. of the Republic, Salto, Uruguay. S.A. Bea, currently at Lawrence Berkeley National Lab., 1 Cyclotron Rd., Berkeley, CA 94720. *Corresponding author (sabea@lbl.gov).

Vadose Zone J.
doi:10.2136/vzj2011.0053
Received 3 June 2011.

Reactive Transport Modeling of Natural Carbon Sequestration in Ultramafic Mine Tailings

Atmospheric CO_2 is naturally sequestered in ultramafic mine tailings as a result of the weathering of serpentine minerals [$Mg_3Si_2O_5(OH)_4$] and brucite [$Mg(OH)_2$], and subsequent mineralization of CO_2 in hydrated magnesium carbonate minerals, such as hydromagnesite [$Mg_5(CO_3)_4(OH)_2{\cdot}4H_2O$]. Understanding the CO_2 trapping mechanisms is key to evaluating the capacity of such tailings for carbon sequestration. Natural CO_2 sequestration in subaerially exposed ultramafic tailings at a mine site near Mount Keith, Australia is assessed with a process-based reactive transport model. The model formulation includes unsaturated flow, equations accounting for energy balance and vapor diffusion, fully coupled with solute transport, gas diffusion, and geochemical reactions. Atmospheric boundary conditions accounting for the effect of climate variations are also included. Kinetic dissolution of serpentine, dissolution-precipitation of brucite and primary carbonates—calcite ($CaCO_3$), dolomite [$MgCa(CO_3)_2$], magnesite ($MgCO_3$), as well as the formation of hydromagnesite, halite (NaCl), gypsum ($CaSO_4{\cdot}2H_2O$), blödite [$Na_2Mg(SO_4)_2{\cdot}4H_2O$], and epsomite [$MgSO_4{\cdot}7H_2O$]—are considered. Simulation results are consistent with field observations and mineralogical data from tailings that weathered for 10 yr. Precipitation of hydromagnesite is both predicted and observed, and is mainly controlled by the dissolution of serpentine (the source of Mg) and equilibrium with CO_2 ingressing from the atmosphere. The predicted rate for CO_2 entrapment in these tailings ranges between 0.6 and 1 kg m^{-2} yr^{-1}. However, modeling results suggest that this rate is sensitive to CO_2 ingress through the mineral waste and may be enhanced by several mechanisms, including atmospheric pumping.

Abbreviations: BET, Brunauer–Emmett–Teller; SWCC, soil water characteristic curve; TIC, total inorganic carbon; TSF, tailings storage facility; XRPD, X-ray powder diffraction.

It is now widely accepted that anthropogenic greenhouse gases, in particular CO_2, have caused most of the increases in global average temperatures since the mid 20th century (IPCC, 2007). Concerns over global climate change provide the motivation for investigating methods to sequester CO_2. Underground CO_2 storage as a supercritical fluid is a widely advocated sequestration strategy (IPCC, 2005); however, fixing carbon within the crystal structures of minerals has also been recognized as a safe and more permanent method for sequestering anthropogenic carbon (e.g., Lackner, 2003; Seifritz, 1990; Wilson, 2009; Wilson et al., 2009). Recent work has shown that CO_2 is naturally sequestered into minerals in deep aquifers, but also at the Earth's surface. Hydrated magnesium carbonate minerals, such as hydromagnesite [$Mg_5(CO_3)_4(OH)_2{\cdot}4H_2O$], are common low-temperature alteration products of serpentine-rich mine wastes (Wilson et al., 2006, 2009; Wilson, 2009). Hydromagnesite, which occurs at Mount Keith, is metastable under Earth surface conditions (Königsberger et al., 1999). However, Power et al. (2009) demonstrated stability of hydromagnesite within alkaline playa deposits in British Columbia, Canada for more than 10 ka. Therefore, if hydromagnesite is stored under neutral to alkaline conditions, dissolution of hydromagnesite and release of CO_2 to the atmosphere is unlikely on the time scale of millennia (Palandri and Kharaka, 2004). Thus, mineralization of CO_2 in ultramafic mine tailings has been proposed as a method by which the mining industry might reduce its greenhouse gas emissions. Understanding the CO_2 trapping mechanisms and quantification of CO_2 capture is key to evaluating how effective ultramafic tailings are for passive carbon sequestration. Process-based reactive transport modeling provides a suitable method to help identify the processes that are responsible for carbon trapping and storage.

Although several reactive transport models have been developed to investigate transport and geochemical processes in the vadose zone of mine tailings (e.g., Xu et al., 2000; Lefebvre et al., 2001a,b; Mayer et al., 2002; Molins and Mayer, 2007; Acero et al., 2009; Bea et al., 2010a), none of these codes account for the full complexity of interactions

between flow and transport processes, energy balance, and geochemical reactions. Most of the existing models focus on the simulation of acid rock drainage (ARD) generation, and only some of the codes recognize dynamic boundary conditions as an important control for assessing the geochemical evolution in tailings (e.g., Xu et al., 2000; Lefebvre et al., 2001a,b; Acero et al., 2009; Bea et al., 2010a). To date, reactive transport modeling has not been applied to investigate CO_2 capture in ultramafic mine waste.

The objective of this contribution is to use reactive transport modeling for a process-based and integrated assessment of CO_2 sequestration in the Mount Keith tailings impoundment, Western Australia (Wilson, 2009). To meet this objective, the multicomponent reactive transport code MIN3P-D (Henderson et al., 2009) is enhanced by including an energy balance equation and vapor transport. An overview on the model development and its verification is also provided in this contribution.

Conceptual Model of Carbon Dioxide Sequestration in Ultramafic Mine Waste

Atmospheric exposure of mine waste containing ultramafic minerals [e.g., serpentine, $Mg_3Si_2O_5(OH)_4$] naturally induces carbon sequestration when Mg released from primary minerals reacts with CO_2 present in the tailings (e.g., Wilson, 2009). Although straightforward in principle, Mg-silicate dissolution and the formation of Mg-hydroxy-carbonates are affected by a variety of interacting processes (Fig. 1).

Under arid conditions, as present at the Mount Keith facility, vadose zone flow in tailings is mainly controlled by low relative humidity in the atmosphere that drives evaporation and causes upward flow of process water. As a result of evaporation, solute concentrations in near surface pore water are dramatically increased, leading to super-saturated conditions with respect to salts and causing the formation of an efflorescent crust (e.g., Stolberg, 2005; Acero et al., 2009; Bea et al., 2010a; Gran et al., 2011). As evaporation progresses, water content and relative permeability near the surface are reduced, inhibiting the flow of water toward the surface. Therefore, the evaporation front is progressively displaced downward, and the region containing efflorescent salts grows with time. As a consequence of evaporation, pH decreases near the tailings surface. This increases the dissolution rate of primary phases [i.e., serpentine and brucite, $Mg(OH)_2$], which become the main source of alkalinity and Mg^{2+} in these tailings (Wilson, 2009; Wilson et al., 2009).

Downward diffusion of CO_2 driven by carbonate precipitation and enhanced by the decrease of water saturation maintains the precipitation of hydrated Mg-carbonates [e.g., hydromagnesite, $Mg_5(CO_3)_4(OH)_2{\cdot}4H_2O$]. As a result, hydrated magnesium carbonate and calcium carbonate minerals mainly occur as near-surface crusts or as disseminated precipitates that cement the tailings pile (Wilson, 2009). The key CO_2 trapping mechanism is based on the following reaction:

$$\underbrace{Mg_3Si_2O_5(OH)_4}_{\text{serpentine}} + 2.4CO_2 + H_2O \Rightarrow 0.6\underbrace{Mg_5(CO_3)_4(OH)_2\cdot 4H_2O}_{\text{hydromagnesite}} + 2SiO_2 \quad [1]$$

In addition, the geochemical evolution of tailings is also affected by the precipitation of other secondary phases. Ca, Mg and Si released from dissolution of primary minerals are reprecipitated in the form of gypsum [$CaSO_4{\cdot}2H_2O$], blödite [$Na_2Mg(SO_4)_2{\cdot}4H_2O$], epsomite [$MgSO_4{\cdot}7H_2O$], and chalcedony [$SiO_2$]. The dissolution and reprecipitation of primary carbonate minerals [i.e., calcite, $CaCO_3$; dolomite, $MgCa(CO_3)_2$; magnesite, $MgCO_3$] may provide another important source or sink of total inorganic carbon (TIC) in the system.

Model Development

The reactive transport code MIN3P (Mayer et al., 2002) was previously enhanced by Henderson et al. (2009) to include the coupling between density driven flow and reactive transport. More recently, an energy balance equation and formulations for reactive transport in high ionic strength solutions were implemented (Bea et al., 2011). As part of this work, the capabilities of the code were further enhanced to include the diffusion of water vapor and atmospheric boundary conditions. A summary of the formulation for vadose zone flow, vapor diffusion, energy balance, and reactive solute and

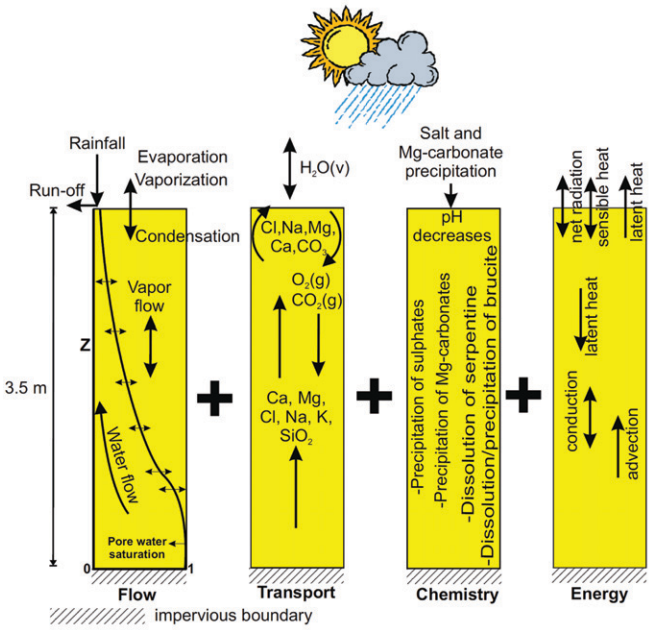

Fig. 1. Conceptual model of carbon dioxide fixation in ultramafic tailings for arid environments.

gas transport is provided below. Additional details of the formulation and constitutive relationships are provided in the Appendix. A verification example for the energy balance equations and water vapor diffusion is also provided in the Appendix.

Vadose Zone Flow and Vapor Diffusion

The implementation of vadose zone flow and vapor diffusion is based on the formulation presented by Philip and De Vries (1957) (see also Saito et al., 2006):

$$\frac{\delta\phi S_l\rho_l}{\delta t}+\frac{\delta\phi S_v\rho_v}{\delta t}=\nabla\cdot q_l+\nabla\cdot q_v+f_w\zeta \qquad [2]$$

where ϕ is the porosity; S_l and S_v are the pore water and vapor saturations, respectively; ρ_l and ρ_v are the pore water and vapor densities [M L^{-3}], t is time [T], q_l and q_v are the water and vapor mass fluxes [M L^{-2} T^{-1}], F_w is a fluid source–sink term [M L^{-2} T^{-1}], and ζ is a constant that relates the surface area on the boundary with the volume of the porous medium [L^2 L^{-3}].

Water fluxes (q_l) in Eq. [2] are calculated based on a modified form of Darcy's Law that includes a thermal hydraulic conductivity term (Noborio et al., 1996; Saito et al., 2006; Sakai et al., 2009):

$$q_l=\rho_l v_l=-\rho_l\frac{Kk_r}{\mu_l}\left[\left(\nabla P_l+\rho_l g\right)+G_{wt}\frac{P_l}{\gamma_0}\frac{\partial\gamma}{\partial T}\nabla T\right] \qquad [3]$$

where v_l is the modified Darcy flux [L T^{-1}], K is the permeability tensor [L^2], k_r is the relative permeability as a function of pore water saturation (S_l), P_l is the pore water pressure [M L^{-1} T^{-2}], g is the gravity constant [L T^{-2}], μ_l is the dynamic fluid viscosity [M L^{-1} T^{-1}], G_{wt} is a gain factor that quantifies the temperature dependence of the soil water retention curve, γ and γ_0 are the water surface tension [M T^{-2}] and its reference value at 25°C (71.89 g s^{-2}), respectively, and T is temperature [°C]. Water fluxes (q_l) in Eq. [3] can be induced by both pressure and temperature gradients.

Vapor fluxes in Eq. [2] take into account the vapor diffusion induced by vapor density (ρ_v) gradients through Fick's equation as:

$$\nabla\cdot q_v=\nabla\cdot\phi S_v\tau_v D_w\nabla\rho_v=\nabla\cdot\phi S_v\tau_v D_w\left(\eta\frac{\partial\rho_v}{\partial T}\nabla T+\frac{\partial\rho_v}{\partial P_l}\nabla P_l\right) \qquad [4]$$

where τ_v is the tortuosity factor (Millington, 1959), D_w is the vapor diffusion coefficient [L^2 T^{-1}], and η is an enhancement factor to describe the increase in thermal vapor flux as a result of liquid islands and increased temperature gradients in the air phase (Cass et al., 1984; Saito et al., 2006; Sakai et al., 2009).

Relationships by Wösten and van Genuchten (1988) are commonly used to describe the pore water saturation and relative permeability as a function of matric suction. In some cases, particularly under very dry conditions, these functions may not represent soil water retention adequately. As an alternative, the enhanced MIN3P code also considers functions proposed by Fayer and Simmons (1995) that extend the functions by Wösten and van Genuchten (1988) to very dry conditions.

Energy Balance Equations

The formulation for energy transport implemented in MIN3P is based on Philip and De Vries (1957) and Voss and Provost (2008):

$$\frac{\delta\phi c_l S_l\rho_l}{\delta t}+\frac{\delta\phi c_v S_v\rho_v}{\delta t}+\frac{\delta(1-\phi)c_s\rho_s}{\delta t}+\frac{\delta L_w\phi S_v\rho_v}{\delta t}=\nabla\cdot j_h+f_h\zeta \qquad [5]$$

where c_l, c_v, and c_s are the heat capacities for liquid, vapor, and solid phases, respectively [E M^{-1} °C^{-1}], $\nabla\cdot j_h$ is the energy flux [E L^{-3} T^{-1}], L_w is the latent heat of vaporization for liquid water [E M^{-1}], and f_h is the energy source–sink term [E L^{-2} T^{-1}]. The energy fluxes term ($\nabla\cdot j_h$) in Eq. [5] is evaluated as:

$$\nabla\cdot j_h=\nabla\cdot c_l q_l T-\nabla\cdot\lambda\nabla T+\nabla\cdot\phi c_l\rho D_h\nabla T+\nabla\cdot c_v q_v T+\nabla\cdot L_w q_v \qquad [6]$$

where λ is the thermal conductivity tensor [E L^{-1} T^{-1} °C^{-1}], and D_h is the thermal dispersion tensor [L^2 T^{-1}].

Reactive Transport Equations

The direct substitution approach is used for solving the coupled multicomponent reactive transport equations for N_c components (Mayer et al., 2002):

$$\frac{\partial}{\partial t}\left(\phi S_l T_j^a\right)+\frac{\partial}{\partial t}\left(\phi S_g T_j^g\right)=\nabla\cdot v_l T_j^a-\nabla\cdot\phi S_l\tau_a D_a\nabla T_j^a-\nabla\cdot\phi S_g\tau_g D_g\nabla T_j^g+Q_j^a+f_j^a+f_j^g \qquad j=1,N_c \qquad [7]$$

where v_l is the Darcy flux (Eq. [3]); T_j^a and T_j^g are the total concentrations for jth component in the aqueous and gas phases, respectively [M L^{-3}]; S_g is the gas phase saturation, τ_a and τ_g are the tortuosities for aqueous and gas phases, respectively, computed here based on the relationships provided by Millington (1959); D_a is the aqueous diffusion–dispersion tensor [L^2 T^{-1}]; D_g is the gas diffusion coefficient in air [L^2 T^{-1}], Q_j^a is the source–sink term for the jth component due to the geochemical reactions [M L^{-3} T^{-1}]; f_j^a and f_j^g are the source–sink terms associated with boundary fluxes for the jth component in the aqueous and gas phases, respectively [M L^{-3} T^{-1}]. This formulation is based on the assumption that gas phase diffusion dominates gas transport, as was suggested by previous studies for similar applications (e.g., Xu et al., 2000; Molins et al., 2008).

Boundary Conditions

To facilitate an adequate description of evaporation under varying climate conditions, atmospheric boundary conditions for flow and energy transport equations have been implemented. Evaporation

E [M L^{-2} T^{-1}], rainfall P [M L^{-2} T^{-1}], and surface run-off J_{sr} [M L^{-2} T^{-1}] are considered through the term f_w (Eq. [2]), which is defined by:

$$f_w = P + E + J_{sr} \quad [8]$$

Evaporation of water from the soil surface is controlled by the exchange of heat between the soil surface and the atmosphere, the flow of water to the soil surface from below, and the transfer of water vapor from the soil surface to the atmosphere. If any of these processes is altered, evaporation will change accordingly. An integrated form of Fick's Law of vapor diffusion accounts for the effects of these three processes. This form of Fick's Law implies that the evaporation rate is equal to the deficit in vapor density between the soil surface and the atmosphere divided by the sum of the atmospheric boundary layer (r_h) and soil surface (r_s) resistances to vapor flow [T L^{-1}]:

$$E = \frac{\left(\rho_v^{atm} - \rho_v\right)}{r_s + r_h} \quad [9]$$

where ρ_v^{atm} is the atmospheric vapor density [M L^{-3}]. If these resistances to vapor flow are not considered, the evaporation rate will be overestimated (Saito et al., 2006).

The present formulation does not account for storage of ponded water; it is assumed that runoff occurs when the precipitation rate exceeds the infiltration capacity of the surface. Note that the evaporation term (E) and the run-off term (J_{sr}) depend on pore water pressure P_l. Runoff is activated if P_l exceeds atmospheric pressure at the ground surface.

The source–sink term for energy transport (f_h in Eq. [5]) is calculated from the surface energy balance (Saaltink et al., 2005; Saito et al., 2006) as:

$$f_h = H_s + L_w E + c_l P T^{atm} + R_n \quad [10]$$

where R_n is the net solar radiation [E L^{-2} T^{-1}] that can be provided as external input based on measured data or calculated internally based on latitude and climate data. Sensible heat flux H_s [E L^{-2} T^{-1}] in Eq. [10], like evaporation, is also described by a diffusion relation accounting for an atmospheric boundary layer:

$$H_s = \rho_g^{atm} c_g \frac{\left(T^{atm} - T\right)}{r_h} \quad [11]$$

where ρ_g^{atm} is the air density [M L^{-3}], and c_g is the heat capacity of air [E M^{-1} °C^{-1}]. The terms $c_l P T^{atm}$ and $L_w E$ in Eq. [10] account for the internal energy of water and vapor fluxes.

Boundary solute and gas fluxes (f_j^a and f_j^g) in Eq. [7] are defined as:

$$f_j^a = J_j^{ab}\left(T_j^{ab}\right) \quad [12]$$

$$f_j^g = J_j^{gb}\left(\nabla T_j^{gb}\right) \quad [13]$$

where J_j^{ab} and J_j^{gb} are the mass fluxes for the jth component in the aqueous and gas phases across the boundary [M L^{-2} T^{-1}]. Boundary fluxes in the aqueous phase are expressed as a function of the total component concentrations (T_j^{ab}), whereas diffusive gas fluxes at the boundary are a function of the gradient of the total concentrations of the jth component in the gas phase (∇T_j^{gb}).

Solution Strategy for Thermohydraulic and Chemical Coupling

The fluid flow conservation and energy transport equations are solved using Newton's method. The coupling between fluid density (i.e., as a function of the temperature) and solute concentrations is solved using the Picard iterative approach. This approach is conceptually straightforward and is used in a number of computer programs that simulate variable density flow and transport problems (Voss, 1984; Ackerer et al., 1999; Diersch and Kolditz, 2002).

Model Parameters for Mount Keith Tailings

The new model capabilities are used for a process-oriented assessment of CO_2 trapping in ultramafic mine tailings located in Western Australia (Mount Keith). Residual material from the processing plant was piped to the tailings storage facilities (TSF1 and TSF2) suspended in hypersaline process water used in the flotation circuit.

Modeling was performed for the TSF1, an experimental tailings impoundment that was in operation from 1994 to 1996 and was sampled in 2006. The tailings are relatively homogeneous in grain size and hydraulic conductivity (Stolberg, 2005), and the impoundment has a large spatial extent in comparison with its thickness. Under these conditions flow and transport processes in the vadose zone are predominantly vertical, and for that reason, the domain is conceptualized as a one-dimensional column composed of 3.5 m sand to clay tailings on the basis of the description reported by Stolberg (2005) (see Fig. 1). This approach has also been used in previous reactive transport modeling studies for tailings by Mayer et al. (2002), Acero et al. (2009), and Bea et al. (2010a). Physical and transport parameters and constitutive laws used in the simulation are shown in Table 1. Estimated soil water characteristic curve (SWCC) parameters describing volumetric water content and hydraulic conductivity were contrasted with site-specific laboratory measurements by Stolberg (2005) and are presented in Fig. 2.

Atmospheric boundary conditions were imposed at the top of the solution domain and impervious boundaries are imposed at the bottom for flow, energy and solute transport. This approach can be justified by the low hydraulic conductivity of the clay foundation ($\sim 10^{-8}$ m s^{-1}, Stolberg, 2005) and near constant temperatures at depth.

Table 1. Physical and transport parameters used in the simulation.

Parameter or constitutive law	Tailings	Reference†
Porosity, ϕ	0.46	1
Hydraulic conductivity K [m s^{-1}]	10^{-8}	1
Retention curve		
α [m^{-1}]	0.8	2
n	1.4	2
S_{rl}	0.001	2
Liquid relative permeability, k_{rl}		
l	1	1
Thermal conductivity, λ [W m^{-1} °C^{-1}]		
b_1 [W m^{-1} °C^{-1}]	0.228	3
b_2 [W m^{-1} °C^{-1}]	−2.406	3
b_3 [W m^{-1} °C^{-1}]	4.909	3
Solid density, ρ_s [kg m^{-3}]	1400	4
Specific heat capacity of solid, c_s (J kg^{-1} °C^{-1})	1100	9
Specific heat of liquid, c_l [J kg^{-1} °C^{-1}]	4182	5
Specific heat capacity of vapor, c_v [J kg^{-1} °C^{-1}]	1996	9
Diffusive transport in the gas phase		
Diffusion coefficient, D_g [m^2 s^{-1}]	1.65×10^{-5}	6
Tortuosity in the gas phase, τ_g [-]	$\tau_g = S_g^{7/3}\phi^{1/3}$	8
Transport diffusion in the aqueous phase		
Diffusion coefficient, D_a [m^2 s^{-1}]	8×10^{-10}	7
Tortuosity in the aqueous phase, τ_a [-]	$\tau_a = S_g^{7/3}\phi^{1/3}$	8
Evaporation by aerodynamic diffusion (E)		
Wind speed, v_a [m s^{-1}]	3.3	9
Screen height, z_a [m]	1	9
Roughness length, z_0 [m]	0.01	9

† 1, Stolberg (2005); 2, fitted from Stolberg (2005); 3, Chung and Horton (1987) and Sakai et al. (2009); 4, computed from the weight percentage and density of the initial mineral content; 5, Voss and Provost (2008); 6, Molins and Mayer (2007); 7, Mayer et al. (2002); 8, computed as Millington (1959); 9, estimated.

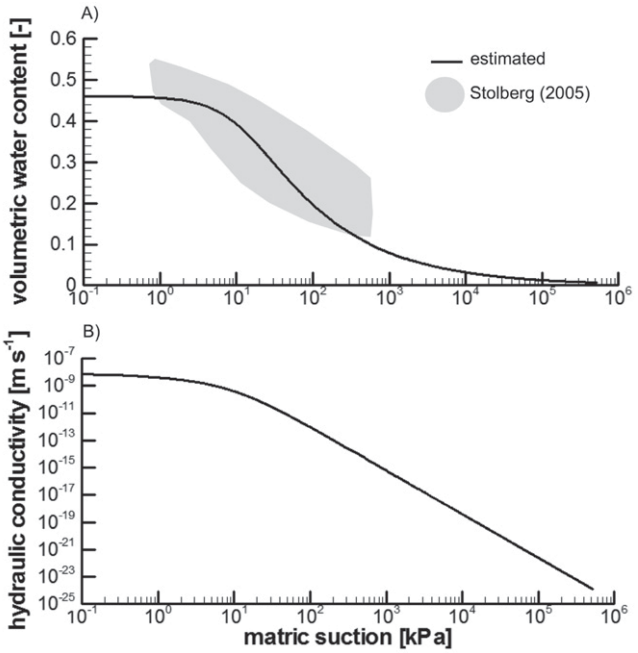

Fig. 2. Model parameters: soil water characteristic curve (SWCC). (A) Measured drying SWCC Mount Keith (TSF1) nickel tailings (Stolberg, 2005) and estimated SWCC used in the present model. (B) Unsaturated hydraulic conductivity function.

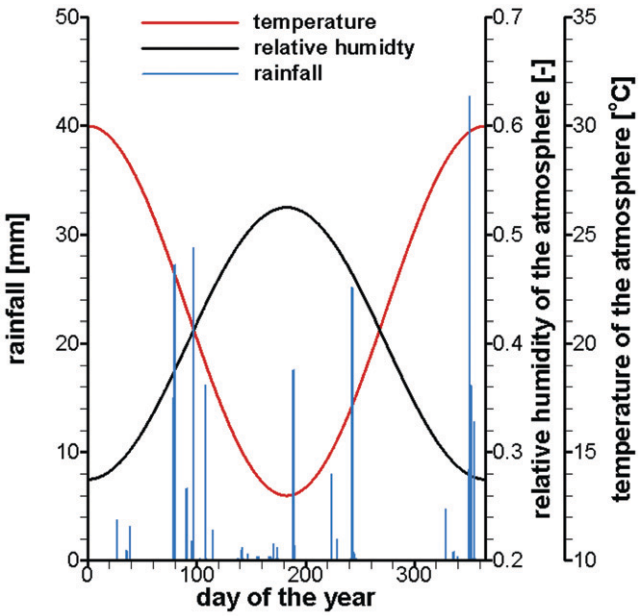

Fig. 3. Atmospheric boundary conditions: temperature and relative humidity of the atmosphere and rainfall imposed in the model. Rainfall events were based on daily data recorded at Leinster Airport (012314 Station, located 60 km south of Mount Keith tailings) for the period 1 Jan. 2010 through 31 Dec. 2010.

As for the atmospheric parameters, maximum and minimum mean values for temperature (T^{atm}) and relative humidity (H_r) were calculated for a period of 30 yr of data recorded in the region. The relative humidity varies between 0.28 and 0.53 and the temperature between 30 and 13°C from summer to winter, respectively. MIN3P allows use of hourly or daily data from a weather station (including precipitation, radiation, temperature, relative humidity, wind speed, cloud cover), but the full weather data records were not available for this site. A simplified approach that captures seasonal fluctuations of temperature and humidity based on sinusoidal functions was used for a time period of 1 yr, as depicted in Fig. 3.

Annual average rainfall for the region is approximately 220 mm and mainly occurs in intense events of short duration (Stolberg, 2005). Daily precipitation recorded in 2010 (1 January–31 December) at the Leinster Airport (station 012314), located 60 km south of the Mount Keith site, were used in the simulations and repeated for a period of 30 yr (Fig. 3). The average duration for

each rainfall event was estimated at 2 h. Wind speed and the presence of cloud cover affect evaporation. In the absence of measured data, a constant wind speed of 3.3 m s^{-1} and a partially cloudy sky were considered in the simulation.

Mineralogy of Mount Keith Tailings

Detailed mineralogical analyses have been conducted for the Mount Keith tailings, providing the data necessary to constrain the reactive transport simulations. The tailings are composed primarily of antigorite and lizardite with hydrotalcite-group minerals (i.e., mostly iowaite and woodallite with occasional pyroaurite, stichtite, and mountkeithite). Minor amounts of brucite, chrysotile, talc, magnetite, chromite, quartz, magnesite, dolomite, and calcite are common (Wilson, 2009). Trace vermiculite is also observed in the tailings. Sulfide minerals have not been detected with X-ray powder diffraction (XRPD) with a detection limit of approximately 0.5% (w/w). Sampling details and analytical methods are described in the Appendix.

Secondary precipitates are abundant in surficial tailings and include carbonate, halide, and sulfate minerals. Efflorescent halide and sulfate minerals are common within the upper 0.25 m of the tailings, although less so in TSF1 than in TSF2. At Mount Keith, halite, hexahydrite, and blödite dominate these efflorescences and are commonly associated with lesser amounts of epsomite, konyaite, löweite, and gypsum. Sanderite, starkeyite, pentahydrite, and carnallite are less common and have only been observed at low abundance. Kainite and anhydrite may or may not be present near detection in very few of the samples analyzed.

Refined abundances and median abundances for hydromagnesite, magnesite, serpentine minerals, dolomite, halite, hydrotalcite-group minerals, brucite, and calcite in 30 samples of 10-yr-old tailings from TSF1 are plotted in Fig. 4. These results were obtained by Rietveld refinement of XRPD data (Appendix 6). Shaded envelopes denote the median plus or minus the median absolute deviation of mineral abundance for depth intervals of 0 to 25, 25 to 50, 50 to 75, 75 to 100, and 100 to 125 cm. Median and median absolute deviation were used as measures of central tendency because Rietveld refinement results produce a sparse set of log-normally distributed data.

Sulfate minerals are restricted to the efflorescences that cover the upper few centimeters of the tailings deposit. Abundances of both hydromagnesite and halite are highest near the surface of TSF1. Abundances of these minerals decrease asymptotically with increasing distance from the surface until they reach relatively constant values at a depth of approximately 0.5 m (Fig. 4).

The abundance data for serpentine, hydrotalcite-group minerals, magnesite, and brucite display a consistent trend toward decreasing abundance with proximity to tailings surfaces. Part of this trend is the result of a first-order change in the composition of tailings during the first few years of mine operation (Wilson, 2009). Another contributing factor is that secondary minerals (i.e., hydromagnesite, halite, and sulfate minerals) in surface efflorescences have precipitated to a large extent from dissolved atmospheric gasses, dissolved aqueous species within process water, and from process water itself. This significant input of crystalline mass that was not contained initially within the processed ore results in a dilution effect in mineral abundances. This occurs because Rietveld refinement results provide a relative measure of crystalline mass, normalized to 100% (w/w).

A second reason for the decrease in the abundance of serpentine (and the virtual disappearance of brucite from surficial tailings) is that these Mg-rich gangue minerals are dissolving and acting as the source of Mg in secondary carbonate and sulfate minerals. Brucite is known to produce hydromagnesite upon weathering under conditions of temperature and pressure that prevail at the Earth's surface (e.g., Hostetler et al., 1966; Xiong and Lord, 2008). Carbonation of 2% (w/w) brucite would produce approximately 3.2% (w/w) hydromagnesite, which would account for >60% of the observed abundance.

Magnesite could also act as a source of Mg for precipitation of hydromagnesite. However, considering that the abundances of two far more soluble carbonate minerals, calcite and dolomite, remain relatively constant with depth it is more likely that the decline in

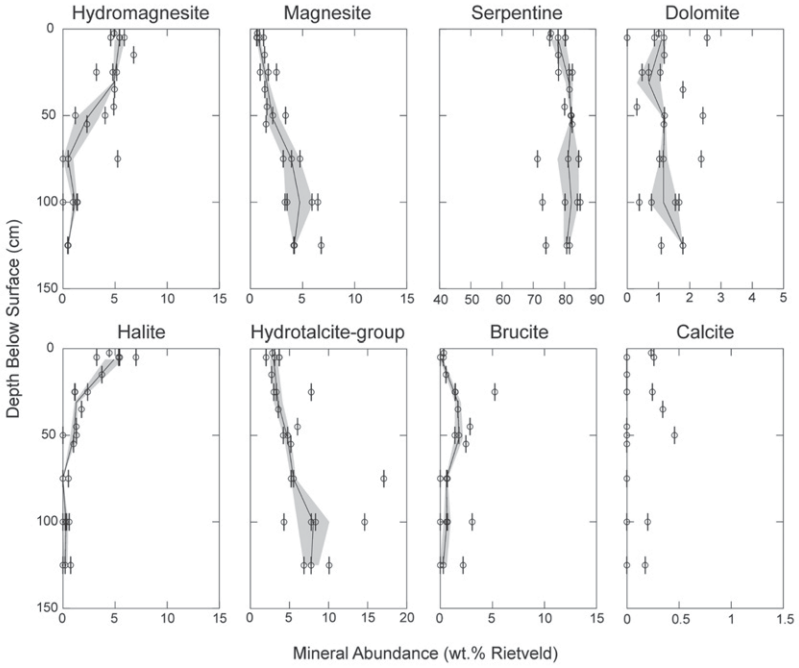

Fig. 4. Variation of select mineral abundances with depth (by Rietveld refinement of X-ray powder diffraction data for 10-yr old tailings from TSF1).

magnesite abundance is related to changes in ore mineralogy. Thus, the observed decrease in the abundances of serpentine and brucite is very likely the result of (i) dissolution to produce secondary Mg-rich minerals and (ii) a dilution effect caused by incorporation of water and atmospheric gasses into these newly formed minerals.

Geochemical System and Composition of Initial and Boundary Waters

A geochemical system consisting of 12 chemical components was considered for describing the main geochemical processes in the Mount Keith tailings: Mg, Ca, Al, Na, K, Si, Cl, TIC, SO_4, H^+, $O_{2(aq)}$, and H_2O. Modeled aqueous species were Ca^{2+}, Mg^{2+}, $MgOH^+$, Na^+, K^+, Al^{3+}, H^+, CO_3^{2-}, HCO_3^-, $CO_{2(aq)}$, $CaCO_{3(aq)}$, $H_2CO_{3(aq)}$, $MgCO_{3(aq)}$, $O_{2(aq)}$, $MgHCO_3^+$, SO_4^{2-}, HSO_4^-, $CaSO_{4(aq)}$, Cl^-, $SiO_{2(aq)}$, H_2O, and OH^-.

Aqueous complexation reactions are assumed to be in equilibrium and are summarized in Table 2. The main heterogeneous reactions considered in the geochemical model are listed in Table 3. Dissolution and precipitation of primary minerals (i.e., serpentine, brucite, dolomite, magnesite, calcite, and hydrotalcite) are modeled using kinetic rate expressions derived from literature data (Table 4). Hydromagnesite, nesquehonite, chalcedony, halite, blödite, hexahydrite, epsomite, and gypsum are included as quasi-equilibrium phases.

The kinetic dissolution rates of the major serpentine polymorphs present at Mount Keith (i.e., antigorite and lizardite) are not well known over the range of pH conditions observed in the mine tailings storage facilities (Stolberg, 2005). Therefore, the dissolution of all serpentine minerals was described using experimental data for chrysotile, which cover the appropriate range of pH (Thom and Dipple, 2005). In these experiments, input solutions with constant pH values (Step 1: pH = 4.4, Step 2: pH = 2.0) were supplied from a reservoir. Two pH-dependent reaction rate expressions for Mg- and Si-poor solutions were proposed (see Table 4). These reaction rates were implemented in the MIN3P database and reaction progress in the experiment was simulated. Simulated results are compared with experimental data in Fig. 5. Dissolution of brucite was experimentally studied by Pokrovsky and Schott (2004). The experimentally determined rates are presented as a function of pH in Fig. 6 together with a fitted rate expression, as defined in Table 4.

The rate expressions from Chou et al. (1989), as shown in Table 4, were used to describe the dissolution of dolomite (precipitation of dolomite was not considered), and dissolution and precipitation of calcite. Magnesite has been reported to form only at temperatures greater than ~60°C and elevated P_{CO2} (Sayles and Fyfe, 1973; Giammar et al., 2005) and was therefore also restricted to an irreversible

Table 2. Geochemical system: homogeneous reactions considered in the simulations.

Homogeneous reactions	$\log_{10} K$ (25°C)
$HSO_4^- \Leftrightarrow H^+ + SO_4^{2-}$	1.98
$MgOH^+ + H^+ \Leftrightarrow H_2O + Mg^{2+}$	−11.81
$OH^- + H^+ \Leftrightarrow H_2O$	−13.1
$CO_{2(aq)} + H_2O \Leftrightarrow CO_3^{2-} + 2H^+$	16.68
$HCO_3^- \Leftrightarrow CO_3^{2-} + H^+$	10.34
$CaCO_{3(aq)} \Leftrightarrow CO_3^{2-} + Ca^{2+}$	3.15
$MgCO_{3(aq)} \Leftrightarrow CO_3^{2-} + Mg^{2+}$	2.93
$MgHCO_3^+ \Leftrightarrow CO_3^{2-} + Mg^{2+} + H^+$	11.4
$H_2CO_{3(aq)} \Leftrightarrow CO_3^{2-} + 2H^+$	16.68

Table 3. Geochemical system: heterogeneous reactions considered in the simulations.

Dissolution/precipitation	$\log_{10} K$ (25°C)
$Chrysotile + 6H^+ \Rightarrow 2H_4SiO_4 + 3Mg^{2+} + H_2O$	†
$Brucite + 2H^+ \Leftrightarrow Mg^{2+} + H_2O$	−17.1 (1)
$Dolomite \Rightarrow Ca^{2+} + Mg^{2+} + 2CO_3^{2-}$	†
$Magnesite \Rightarrow Mg^{2+} + CO_3^{2-}$	†
$Calcite \Leftrightarrow Ca^{2+} + CO_3^{2-}$	8.46‡
$Hydrotalcite + 16H^+ \Rightarrow 6Mg^{2+} + CO_3^{2-} + 2Al^{3+} + 16H_2O$	†
$Chalcedony + 2H_2O \Leftrightarrow H_4SiO_4$	3.52‡
$Hydromagnesite + 2H^+ \Leftrightarrow 4\,CO_3^{2-} + 5Mg^{2+} + 6H_2O$	8.77‡
$Nesquehonite \Leftrightarrow CO_3^{2-} + Mg^{2+} + 3H_2O$	5.17‡
$Halite \Leftrightarrow Na^+ + Cl^-$	−1.58‡
$Blödite \Leftrightarrow 2Na^+ + Mg^{2+} + 2SO_4^{2-} + 4H_2O$	2.48‡
$Hexahydrite \Leftrightarrow Mg^{2+} + SO_4^{2-} + 6H_2O$	1.67‡
$Epsomite \Leftrightarrow Mg^{2+} + SO_4^{2-} + 7H_2O$	2.14‡
$Gypsum \Leftrightarrow Ca^{2+} + SO_4^{2-} + 2H_2O$	4.58‡
Gas dissolution/exsolution	
$O_{2(g)} \Leftrightarrow O_{2(aq)}$	2.9
$CO_{2(g)} \Leftrightarrow CO_3^{2-} - H_2O + 2H^+$	18.16

† Irreversible dissolution.
‡ Reversible reaction (dissolution/precipitation).

Table 4. Kinetic rate expressions used in the simulations. Hydromagnesite, nesquehonite, halite, chalcedony, blödite, epsomite, gypsum and hexahydrite were considered as quasi-equilibrium reactions.

Reaction process	Rate expression	Fitted calibration factor (f_c)	Reference†
	mol L^{-1} s^{-1}		
Chrysotile dissolution (Mg path)	$R_i = S_i \times 10^{-10.02} a_{H+}^{0.22}$	0.035	1
Chrysotile dissolution (Si path)	$R_i = S_i \times 10^{-10.37} a_{H+}^{0.19}$		
Brucite	$R_i = S_i \times 10^{-6.38} a_{H+}^{0.2} (1-\Omega_i^2)$	0.05	2
Magnesite dissolution	$R_i = S_i \left(10^{-6.38} a_{H+}^{0.589} + 10^{-9.34}\right)$	0.01	3
Dolomite dissolution	$R_i = S_i \left(10^{-2.58} a_{H+}^{0.75} + 10^{-4} a_{CO2(aq)}^{0.75} + 10^{-7.66}\right)$	0.001	4
Calcite	$R_i = S_i \left(10^{-0.051} a_{H+} + 10^{-6.19} a_w + 10^{-3.301} a_{H2CO3(aq)}\right)(1-\Omega_i)$	1	4
Hydrotalcite	$R_i = S_i \times 10^{-9} a_{H+}^{0.5}$	1	5

† 1, Thom and Dipple (2005); 2, estimated based on data presented by Pokrovsky and Schott (2004); 3, Palandri and Kharaka (2004); 4, Chou et al. (1989); 5, estimated from field observations presented by Wilson (2009).

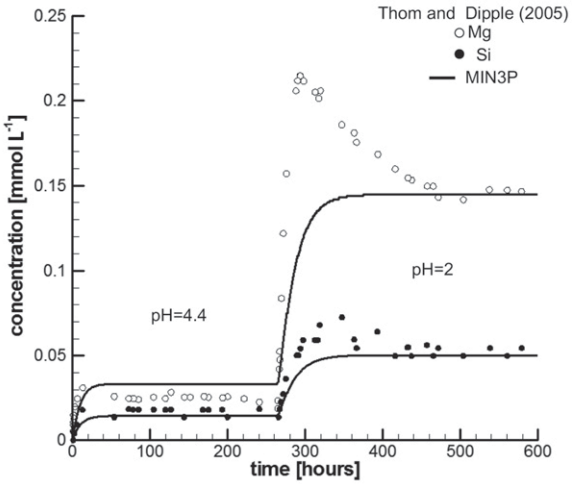

Fig. 5. Chrysotile dissolution rate: temporal evolution of Mg and Si effluent concentrations during chrysotile dissolution experiment (measured data from Thom and Dipple, 2005). Continuous lines show the results obtained by MIN3P.

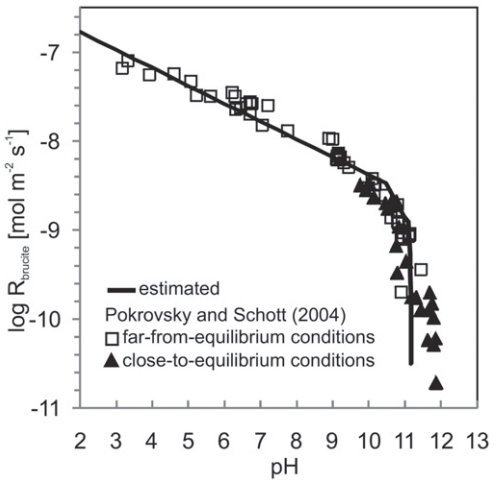

Fig. 6. Estimated brucite [$Mg(OH)^2$] dissolution rate ($R_{brucite}$) as a function of pH (Table 4), measured data from Pokrovsky and Schott (2004).

dissolution reaction. The rate expression for magnesite dissolution was taken from Palandri and Kharaka (2004), based on experimental data reported by Pokrovsky and Schott (1999) (Table 4).

In the model, the initial mineralogy is composed of a mixture of serpentine, brucite, and carbonates (magnesite, calcite, dolomite, and hydrotalcite; Table 5). The volumetric fraction occupied by each mineral is calculated from its weight fraction by considering its density. Weight fractions are estimated using Rietveld refinement results for XRPD data on samples from the Mount Keith tailings (Fig. 4 and Wilson, 2009). Total surface area for each mineral S_i [m^2 L^{-1}] in Table 4 is computed based on its weight fraction percentage $wt\%_i$, bulk solid density ρ_s [g L^{-1}], and reactive surface area σ_i [m^2 g^{-1}] shown in Table 5 as:

$$S_i = \frac{wt\%_i \rho_s \sigma_i}{100} \quad [14]$$

being the reactive surface (σ_i) calculated as the product of the measured surface area (Table 5) times a fitted calibration factor f_c (Table 4). This fitted calibration factor represents the ratio between the mineral specific surface areas derived from the Brunauer–Emmett–Teller (BET) measurements and the reactive surface areas used in the present model. Effective reactive surface areas are typically one to three orders of magnitude lower than surface areas derived from BET measurements, which is in line with previous observations (White and Peterson, 1990). The chemical compositions for the initial and boundary solutions are shown in Table 6. The initial pore water composition is derived from the hypersaline process water emplaced with the tailings; the total concentrations for Ca, TIC, and Mg were modified by equilibrium with calcite,

Table 5. Initial mineralogy considered in the simulations.

Mineral phase	Weight	Volume	Measured surface area	Reactive surface area[5] σ
	%		$m^2\ g^{-1}$	
Chrysotile	85.75	46.17	17.6[1]†	0.616
Brucite	2.5	1.44	0.12[2]	0.006
Dolomite	1.5	0.72	0.069[3]	6.9×10^{-5}
Magnesite	5	2.21	0.066[3]	6.6×10^{-4}
Calcite	0.25	0.13	0.037[3]	0.037
Hydrotalcite	5	3.33	10[4]	10
Chalcedony	0	0		
Hydromagnesite	0	0		
Nesquehonite	0	0		
Halite	0	0		
Blödite	0	0		
Hexahydrite	0	0		
Epsomite	0	0		
Gypsum	0	0		
Total	100	54		

† Methods: (1) BET (Thom and Dipple, 2005), (2) BET (Pokrovsky and Schott, 2004), (3) BET (Pokrovsky et al., 2005), (4) Calculated from the specific surface and the weight content of the primary solid phases of the concrete and the argillite (De Windt et al., 2008), and (5) Calculated as the product between the measured surface area times the fitted calibration factor (f_c) shown in Table 4.

Table 6. Chemical compositions for initial and boundary solutions.

	Initial solution	Boundary solution
pH	9.75	6
Ca, mol L^{-1}	9.7×10^{-4}	1.1×10^{-3}
Mg, mol L^{-1}	6.8×10^{-2}	7.4×10^{-4}
Na, mol L^{-1}	1	7.5×10^{-3}
K, mol L^{-1}	3.3×10^{-2}	1.5×10^{-4}
Cl, mol L^{-1}	1	7.5×10^{-3}
SO_4, mol L^{-1}	8.5×10^{-2}	1.9×10^{-3}
O_2, mol L^{-1}	1.8×10^{-4}	2.6×10^{-4}
Si, mol L^{-1}	10^{-4}	–
TIC, mol L^{-1}	6.9×10^{-4}	2.7×10^{-5}
Al, mol L^{-1}	10^{-10}	10^{-10}
Ionic strength, mol L^{-1}	1.32	0.014
P_{CO2}, atm	7.2×10^{-7}	3.4×10^{-4}
P_{O2}, atm	0.21	0.21
Mineral saturation indices		
SI_{Bru}	0	−9.06
SI_{Hymg}	0	−34.57
SI_{Hal}	−1.97	−5.94
SI_{Cal}	0	−4.33

hydromagnesite and brucite, respectively (note that the resulting P_{CO2} was lower than atmospheric). The boundary condition for solute transport was based on the chemical composition of meteoric water taken from Bea et al. (2004) in equilibrium with the partial pressure of $CO_{2(g)}$ in the atmosphere ($\approx 3.4 \times 10^{-4}$ atm). For both solutions, equilibrium with atmospheric oxygen (P_{O2} = 0.21 atm; Mayer et al., 2002) is assumed. Speciation calculations were performed with the help of the CHEPROO code (Bea et al., 2009). Considering the hypersaline nature of the pore water in these tailings (>50,000 mg L^{-1} total dissolved solids, Stolberg, 2005), the Pitzer ion interaction approach was used for the calculation of the aqueous activities (the HMW model, Harvie et al., 1984; Bea et al., 2010b). Virial coefficients for most of the ions were taken from Harvie et al. (1984) at 25°C and 1 atm.

Modeling Results

Simulations were conducted for a time period of 30 yr and the predicted thermohydraulic, and geochemical evolution and an estimation of CO_2 uptake are described in the following sections. Despite the fact that results for a simulation time of 10 yr were consistent with the data set of observations in Mount Keith tailings, the simulation time was extended to 30 yr, which is consistent with the predicted lifetime of the Mount Keith mine (from commencement of operations to closure). Thus, the extrapolation of the model to 30 yr provides an estimate of carbon mineralization over the operational lifetime of the mine.

Thermohydraulic Evolution

Vertical distributions for water content, temperature, vapor density, and matric suction at different times are shown in Fig. 7; the temporal evolution for temperature, matric suction, and vapor density at 0.05 m below the tailings surface are shown in Fig. 8 for a time period of 10 yr.

Due to arid conditions with very limited precipitation, the water content of the initially saturated tailings decreases as evaporation progresses (Fig. 7). The normalized bulk water content contained in the 3.5-m-thick tailings column decreases by 30% during 10 yr (Fig. 8C). Temperatures at depth quickly approach yearly average temperatures of approximately 22°C and reflect seasonal fluctuations near the ground surface (Fig. 7 and Fig. 8A). Pore water pressures decline substantially near the ground surface (Fig. 7) due to the development of very dry conditions.

As expected, the temperature on the tailings surface declines during the winter months, closely following decreases in solar radiation and air temperature (compare Fig. 3 and Fig. 8). Near surface temperatures in the tailings are higher than the atmospheric temperature (Fig. 8) with larger discrepancies during the summer months, and a slight increase over time. These observations can be

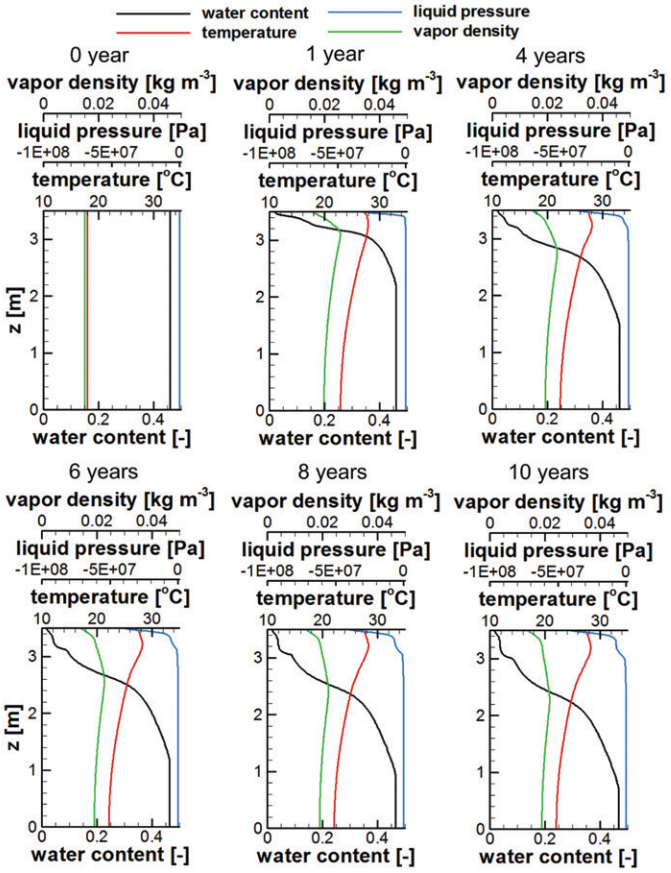

Fig. 7. Modeling results: water content, liquid pressure, vapor density, and temperature distributions at 0, 1, 4, 6, 8, and 10 yr, respectively.

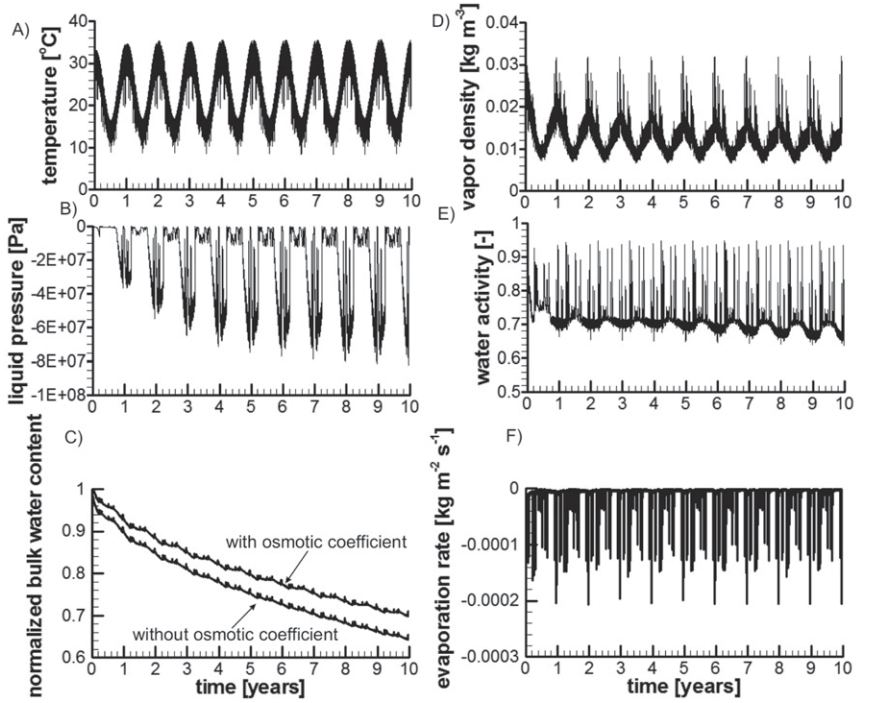

Fig. 8. Modeling results for flow, vapor transport, and energy balance: (A) temporal evolution of temperature, (B) liquid pressure, (D) vapor density, and (E) water activity at 0.05 m below the tailings surface. Temporal evolution of (C) the normalized bulk water content for the entire tailings thickness and (F) evaporation rate at the tailings surface are also shown.

explained by considering the energy balance at the upper boundary. Most of the incoming radiation is consumed by evaporation of water. However, the mean evaporation rate decreases over time as very dry conditions develop near the tailings surface (Fig. 7), implying decreases in water activity and in liquid pressure near the surface (see Fig. 8B, E and F). As a result, the latent heat flux (related to evaporation) declines over the years. To maintain the heat balance, the sensible heat flux has to increase over time, which requires an increase in the difference between the surface and air temperature, which can only be achieved by a temperature increase of the surficial tailings.

Although vertical vapor density distribution is generally correlated with the temperature distribution, vapor density decreases dramatically near the surface because of dry conditions and high suction (Fig. 7). Simulation results show that rainfall events temporarily impact bulk water content in these tailings (Fig. 8C); however, the net water loss dominates long-term evolution. Evaporation rates increase during the summer when the relative humidity decreases, but also increase following rainfall events as the liquid saturation, vapor density, and water activity increase near the tailings surface (see Fig. 8F).

An alternative simulation, for which the vapor density (ρ_v) was not corrected by the osmotic suction [i.e., through water activity (a_w), the impact of which on the evaporation rate can be found in Krumgalz et al. (2000) and Gamazo et al. (2011)] was also conducted (see Fig. 8C). Results suggest that neglecting osmotic effects would tend to overestimate long-term water loss (35% instead of 30% when including the osmotic correction term).

Evolution of Pore Water Composition and $P_{CO2(g)}$

The vertical distributions of total concentrations for Cl, Na, Mg, SO_4, and TIC at different times are shown in Fig. 9. Ion concentrations progressively increase due to solute transport toward the ground surface, and subsequent water content decreases as a result of evaporation. The same trend is also observed for K and Ca (results not shown). However, TIC quickly reaches a steady state at the beginning of the simulation.

The distribution of pH is maintained in an alkaline range (between 8 and 10, see Fig. 10) as was observed in these tailings (Stolberg, 2005). However, despite the fact that the initial pH was 9.75 (see Table 6), simulations suggest that pH progressively decreases toward 8 to 9 near the surface. This decrease is due to an up-concentration of protons, as evaporation proceeds; however, the

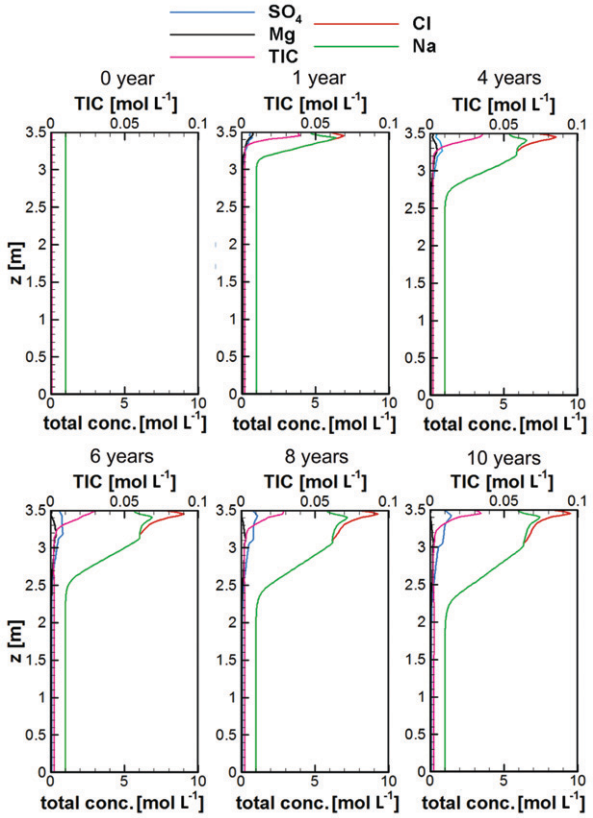

Fig. 9. Modeling results of geochemical evolution: vertical distribution of concentrations for Cl, Na, Mg, SO_4, and total inorganic carbon (TIC) at different times (0, 1, 4, 6, 8, and 10 yr, respectively).

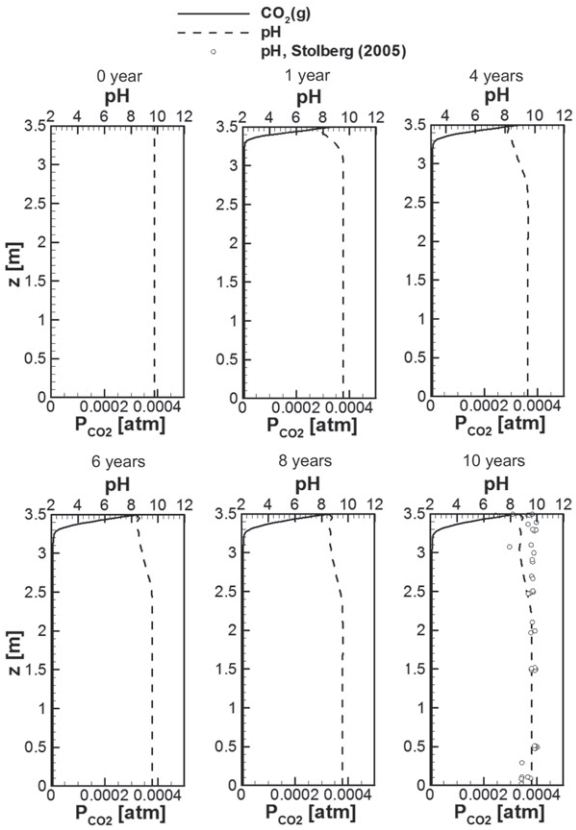

Fig. 10. Modeling results of geochemical evolution: vertical distribution of $P_{CO2(g)}$ (atm) and pH at different times. pH measurements corresponding to November 2001 were taken from Stolberg (2005).

pH decrease is buffered by the dissolution of serpentine, brucite, and hydrotalcite.

The vertical distribution of CO_2 partial pressure at different times is also shown in Fig. 10. The P_{CO2} profile quickly reaches a quasi-steady state, and carbon dioxide pressure declines from atmospheric concentrations at the surface (3.4×10^{-4} atm) to values of approximately 5×10^{-5} atm at a depth of 0.5 m. These conditions develop due to the precipitation of hydrated magnesium carbonate mineral phases and the downward concentration gradient leads to a sustained ingress of atmospheric CO_2.

Formation of Magnesium-Hydrated Carbonates and Other Secondary Phases

The modeled vertical distributions of serpentine, brucite, hydromagnesite, and halite at different times (0, 1, 4, 6, 8, and 10 yr, respectively) are shown in Fig. 11. The dissolution of serpentine is predicted to occur throughout the entire tailings, releasing Mg. However, the rate of dissolution increases as pH decreases in the evaporation zone (Fig. 10 and Fig. 11).

For brucite, the simulations suggest that dissolution occurs in the evaporation zone of the tailings as pH progressively decreases, whereas brucite precipitation is predicted in the deeper sections of the tailings zones, where the pH is greater

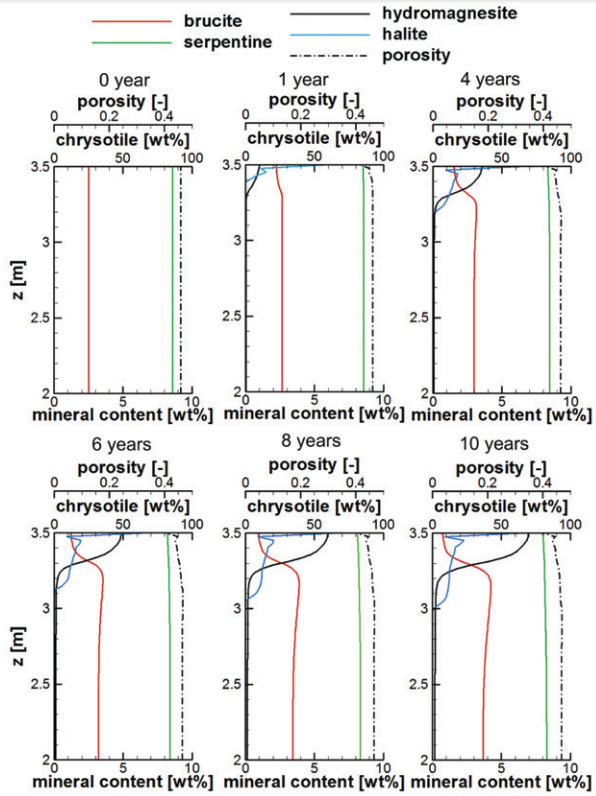

Fig. 11. Modeling results of mineralogical evolution: vertical distribution of mineral contents for serpentine, brucite, hydromagnesite and halite at different times. Porosity distributions are also shown.

than 9. Brucite precipitation in this region is partly driven by serpentine dissolution.

Precipitation of hydromagnesite and halite are also predicted in the evaporation zone of these tailings, and the precipitation fronts migrate to deeper regions as evaporation progresses (Fig. 11). The concentration of hydromagnesite increases over time, suggesting continued sequestration of CO_2 from the atmosphere and from brucite dissolution, whereas halite practically remains constant (Fig. 11). Halite is partially redistributed in the surficial tailings due to reoccurring rainfall events. Precipitation of small amounts of nesquehonite is also predicted in this zone (results not shown). In addition, blödite is precipitating in the evaporation zone (Fig. 12E), whereas chalcedony precipitates throughout the tailings (results not shown).

Simulation results suggest limited reactivity of primary carbonates (i.e., calcite, dolomite, and magnesite), despite the fact that calcite is allowed to dissolve and precipitate. Porosity is practically unaffected over time, despite the formation of an efflorescent crust and the dissolution of serpentine (Fig. 11).

Estimation of Carbon Dioxide Trapping in Mount Keith Tailings

An estimate of cumulative CO_2 trapping in the Mount Keith tailings over a period of 30 yr is shown in Fig. 13 (for 1994–2024). The calculation is based on simulated gas fluxes across the tailings surface with an arithmetic average of about 0.4 μmol m^{-2} s^{-1} from the atmosphere toward the tailings, decreasing from 0.51 to 0.31 μmol m^{-2} s^{-1} during the 30-yr simulation period (calculated based on 5-yr averages).

The simulations indicate that 17 kg m^{-2} of CO_2 are trapped in the tailings mostly by hydromagnesite precipitation after 30 yr (Fig. 13). However, comparison of the simulated hydromagnesite accumulation with observed data (Fig. 12B) suggests that simulations have underpredicted hydromagnesite formation considerably. The simulations were conducted with a CO_2 diffusion coefficient in air of 1.65×10^{-5} m^2 s^{-1}, which is representative for the average yearly temperature at Mount Keith, and high pore gas saturations. It is conceivable that additional processes that were not considered in the simulations may lead to enhanced ingress of CO_2. Processes not considered include the temperature dependence of diffusion coefficients, gas advection due to barometric pressure fluctuations (Massmann and Farrier, 1992), advective CO_2 displacement in the gas phase due to displacement by ingressing precipitation water, and wind effects. In an attempt to better match observed hydromagnesite formation, an additional simulation was conducted with $D_g = 6 \times 10^{-5}$ m^2 s^{-1} (Fig. 12B), using CO_2 diffusion as a surrogate for all processes affecting CO_2 transport. In this case, the simulations predict that 31 kg m^{-2} of CO_2 are trapped in the tailings over a 30-yr time period (Fig. 13). An enhanced CO_2 diffusion coefficient also impacts brucite distribution (see Fig. 12C). Its

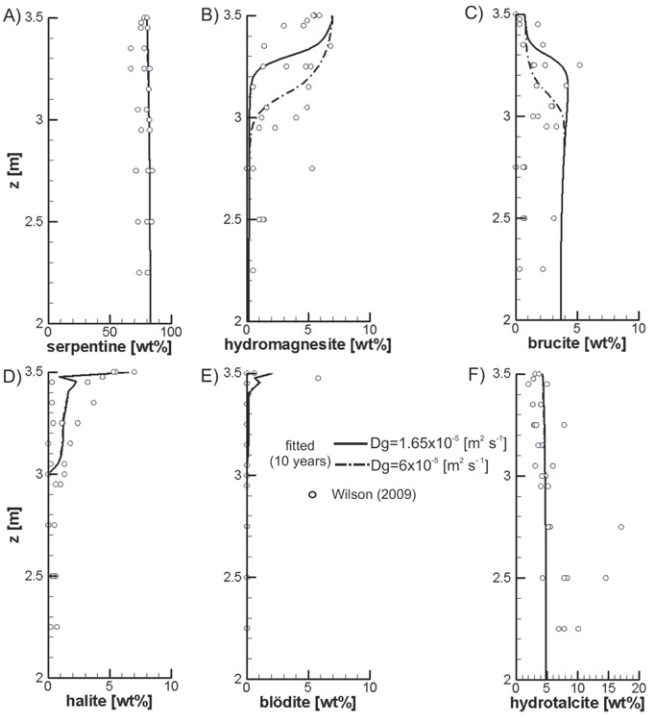

Fig. 12. Modeling results of mineralogical evolution: Vertical distribution for (A) serpentine, (B) hydromagnesite, (C) brucite, (D) halite, (E) blödite, and (F) hydrotalcite after 10 yr ($D_g = 1.65 \times 10^{-5}$ [m^2 s^{-1}], solid line; $D_g = 6 \times 10^{-5}$ [m^2 s^{-1}], dashed line). Results are compared with observations corresponding in the TSF1 storage facility (Wilson, 2009).

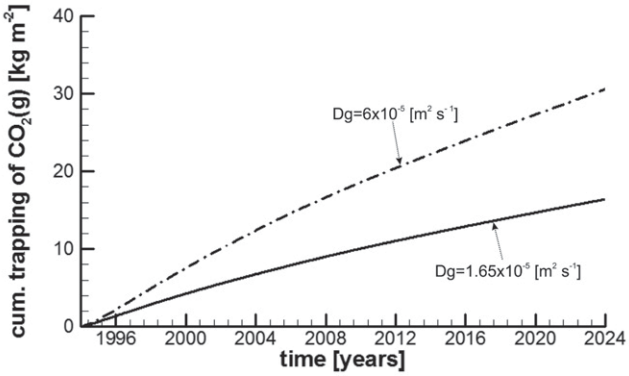

Fig. 13. Modeling results: Cumulative CO_2 trapping in Mount Keith tailings, computed based on total CO_2 flux across tailings surface (solid line). Dashed line corresponds to results for CO_2 gas diffusion coefficient of 6×10^{-5} [m^2 s^{-1}].

dissolution front reaches deeper portions in these tailings, whereas the remaining mineral distributions (i.e., serpentine, halite, blödite, and hydrotalcite) keep invariant (Fig. 12A, D, E, and F).

The results indicate that 3.4% (w/w) of serpentine was dissolved in 10 yr near the surface of the tailings with lower consumption rates in deeper sections, suggesting that the material possesses long-term sequestration potential. The dissolution of serpentine at depth is

likely an artifact of how the dissolution rate law was implemented, that is, as an irreversible reaction. However, this simplification does not affect the carbonation rates in the surficial region of the tailings where far-from-equilibrium conditions prevail. The primary conclusions of this study regarding CO_2 uptake therefore remain unaffected.

Discussion and Concluding Remarks

The laboratory-determined serpentine dissolution rate had to be reduced using a factor of 0.035 (see Table 4) to obtain a consistent result with the observations (see Fig. 12A). This reduction may be justified due to hydromagnesite precipitation on the surface of serpentine (Wilson et al., 2009; Wilson, 2009), which reduces its reactivity (i.e., passivation by "coating" is not simulated here). However, this adjustment is in line with previous studies that investigated the relationship between theoretical and effective reactive surfaces (e.g., White and Peterson, 1990). Under field conditions, the reduction of reactive surface areas may also be due to preferential flow effects and reduced contact between pore water and mineral surfaces (e.g., Lichtner and Kang, 2007).

As was suggested by Wilson (2009), the dissolution of brucite [$Mg(OH)_2$] serves as a secondary source of Mg, as pH drops in the evaporation zone. This process was confirmed by the model for the surficial region of the tailings; however, the simulations also suggest precipitation of brucite in the deeper regions that remain at elevated pH values between 9 and 10.

The precipitation of efflorescent salts such as halite and blödite are also predicted in the upper part of the tailings, consistent with observations for TSF1 (Fig. 4 and Fig. 12D and E; Wilson, 2009). Despite that Cl and Na are present at comparable concentrations at the beginning of the simulation, Na concentrations decrease close to the tailings surface as blödite starts to precipitate (i.e., it consumes Na, and a chemical divide is produced; see, e.g., Bea et al., 2010a).

The simulated pH profiles are largely unaffected over time and remain in the alkaline range (between 8 and 10), as was observed in previous investigations (e.g., see Fig. 10 corresponding to 10 yr; Stolberg, 2005). The progressive pH decrease toward neutral values near the tailings surface is attenuated by the dissolution of serpentine and brucite, which provide a key source of alkalinity in these tailings. However, observations and simulation results also suggest that the kinetic dissolution of hydrotalcite (not very well documented in the literature) may be another potential source of alkalinity in these tailings.

The assumption to reduce the reactivity of bedrock-carbonates in the present model is consistent with observations at Mount Keith, where there is strong evidence that bedrock carbonate minerals are not being dissolved and remineralized (Wilson, 2009).

Simulations and field observations indicate that 17 to 31 kg m^{-2} of $CO_{2(g)}$ become trapped in the tailings over a time period of 30 yr (Fig. 13). Model-predicted sequestration displays only a limited decrease over time because the mineral content and reactive surface area of serpentine are only slightly altered over the 30-yr simulation period. The modeling results suggest that the trapping capacity for carbon dioxide may be maintained for decades in these tailings. The results also indicate that diffusive ingress of atmospheric carbon dioxide from the tailings surface plays an important role for carbon fixation (Fig. 13). In addition, the fact that model results predict a lower CO_2 uptake than indicated by mineralogical data suggests that additional transport processes enhance carbon capture.

The mechanistic reactive transport modeling approach has demonstrated that complex physical and chemical processes play a role for CO_2 capture in ultramafic tailings in arid environments. Overall, good agreement was obtained between field observations and model simulations; however, the measurement of CO_2 fluxes, concentrations gradients, and moisture contents within the tailings would greatly help to confirm findings derived from previous studies focusing on mineralogical alteration, including hydromagnesite precipitation.

The implementation of carbon mineralization at industrial point sources requires high pressures and temperatures due to short residence times and timescales (e.g., hours) (Sipilä et al., 2008). This strategy remains both energy-intensive and expensive and is, therefore, not broadly implemented. Our results suggest that passive sequestration technologies, such as mineral carbonation in mine tailings, offer a low-temperature, low-pressure alternative—exploiting the natural process of silicate weathering to enhance capture and storage of CO_2 in the form of carbonate minerals.

Appendix

Constitutive Relationships for Vadose Zone Flow

Solution density, viscosity, and surface tension in Eq. [3] are affected by changes in temperature and solution composition. Fluid density (ρ_l) is evaluated as:

$$\rho_l = \rho_f + \Delta\rho_C + \Delta\rho_T \qquad [A1]$$

where ρ_f is the reference density (e.g., freshwater at 25°C) [M L^{-3}], and $\Delta\rho_C$ and $\Delta\rho_T$ are the density changes due to solution composition and temperature, respectively [M L^{-3}]. The dependence of density on solution composition ($\Delta\rho_C$) can be approximated by a linear relationship between density and total dissolved solid or is

calculated using Pitzer's ion interaction model following Monnin (1994). Density changes due to temperature ($\Delta\rho_T$) are defined as:

$$\Delta\rho_T = \frac{\partial\rho}{\partial T}\Delta T \quad [A2]$$

where $\partial\rho/\partial T$ is a constant that describes the density dependence on temperature [M L^{-3} °C^{-1}], and ΔT is the temperature change [°C]. Dynamic fluid viscosity (μ_l) is expressed as a function of solution composition and temperature (Lever and Jackson, 1985; Kolditz et al., 1998):

$$\mu_l = \mu_f f_C^{\mu} f_T^{\mu} \quad [A3]$$

with

$$f_C^{\mu} = \frac{1+1.85\omega+4.1\omega^2+44.5\omega^3}{1+1.85\omega_f+4.1\omega_f^2+44.5\omega_f^3} \quad [A4]$$

and

$$f_T^{\mu} = \frac{1+0.7063\sigma_f-0.04832\sigma_f^3}{1+0.7063\sigma-0.04832\sigma^3} \quad [A5]$$

where $\sigma = (T - 150)/100$ (T, °C) and ω is the solute mass fraction in the fluid and ω_f is the solute mass fraction of the fluid at the reference viscosity μ_f). Surface tension (γ) is computed as a function of temperature (Saito et al., 2006; Sakai et al., 2009):

$$\gamma = 75.6 - 0.1425T - 2.38 \times 10^{-4} \quad [A6]$$

Constitutive Relationships for Vapor Transport

The vapor diffusion coefficient D_w [L^2 T^{-1}] is computed as a function of temperature (T, °C) according to Saito et al. (2006):

$$D_w = 2.12\times10^{-5}\left(\frac{T}{273.15}\right)^2 \quad [A7]$$

The enhancement factor η in Eq. [4] is defined as (Cass et al., 1984; Saito et al., 2006; Sakai et al., 2009):

$$\eta = a+3S_l-(a-1)e^{-\left[\left(1+\frac{2.6}{\sqrt{f_c}}\right)S_l\right]^4} \quad [A8]$$

where fc is the mass fraction of clay in the soil, and a is an empirical constant (Sakai et al., 2009).

Vapor density (ρ_v) calculations in Eq. [2] and Eq. [4] account for the effect of capillary pressure (through relative humidity H_r) and salinity as a function of water activity a_w (e.g., see Saaltink et al., 2005):

$$\rho_v = \rho_{sv} H_r a_w \quad [A9]$$

where ρ_{sv} is the temperature-dependent saturated vapor density [M L^{-3}]. Relative humidity (H_r) is derived the from pore water pressure and temperature following Philip and De Vries (1957):

$$H_r = e^{-\left[\frac{(P_{atm}-P_l)M_w}{\rho_l RT}\right]} \quad [A10]$$

where P_{atm} is the atmospheric pressure [Pa], and R the universal gas constant (8.314 [m^3 Pa mol^{-1} K^{-1}]). The saturated vapor density (ρ_{sv}) in Eq. [A9] can be computed in two ways: the first option is based on the psychrometric law as a function of vapor pressure (ρ_v, Pa) (e.g., see Edlefson and Anderson, 1943; Olivella et al., 1994; Saaltink et al., 2005):

$$\rho_{sv} = \frac{M_w P_v}{RT} \quad [A11]$$

where P_v is defined as a function of temperature:

$$P_v = 1.36075\times10^{11} e^{-\frac{5239.7}{T}} \quad [A12]$$

Alternatively, ρ_{sv} can be calculated as proposed by Saito et al. (2006):

$$\rho_{sv} = 10^{-3}\frac{e^{31.3716-\frac{6014.79}{T}-7.92495\times10^{-3}}}{T} \quad [A13]$$

Due to the presence of concentrated brines in the pore water, water activity (a_w) in Eq. [A9] is evaluated based on the HMW model (Harvie et al., 1984; Bea et al., 2010b).

Constitutive Relationships for Energy Transport

Latent heat of vaporization (L_w) in Eq. [5] is defined as a function of temperature:

$$L_w = 2.501 \times 10^6 - 2369.2T \quad [A14]$$

Various expressions are available in the literature to compute the thermal conductivity λ in Eq. [6]. Here, λ is calculated as a function of pore water saturation (S_l) following Chung and Horton (1987); Sakai et al. (2009):

$$\lambda(S_l) = b_1 + b_2\phi S_l + b_3(\phi S_l)^{0.5} \quad [A15]$$

where b_1, b_2, and b_3 are constants [E L^{-1} T^{-1} °C^{-1}]. Other expressions are also available in MIN3P (Voss and Provost, 2008):

$$\lambda(S_l) = \phi S_l\lambda_l + (1-\phi)\lambda_s \quad [A16]$$

where λ_l and λ_s are the liquid and solid thermal conductivities, respectively [E L^{-1} T^{-1} °C^{-1}].

Constitutive Relationships for Atmospheric Boundary Conditions

Two options, both depending on soil water content, are implemented to account for the effect of soil surface resistance (r_s) on vapor diffusion (Eq. [9]). The formulation of Bittelli et al. (2008) is defined by:

$$r_s = 3.5\left(\frac{1}{S_l}\right)^{2.3} + 33.5 \qquad [A17]$$

Alternatively, the formulation proposed by Simunek et al. (2009) can be used:

$$r_s = r_{s0} e^{36.5\phi(S_l - S_{l0})} \qquad [A18]$$

where r_{s0} is the soil resistance on the soil surface [T L^{-1}] and S_{l0} is the minimal residual saturation.

Aerodynamic resistance (r_h) in Eq. [9] is computed as (Saito et al., 2006; Bittelli et al., 2008):

$$r_h = \frac{\left[\ln\left(\frac{z_a + z_0}{z_0}\right) + \theta\right]^2}{k^2 v_a} \qquad [A19]$$

where k is the Von Karman's constant (~0.4), θ is a stability factor, z_0 is the roughness length [L], v_a is the wind velocity [L T^{-1}], and z_a [L] is the elevation above ground surface at which v_a and ρ_v^{atm} are measured.

Solar radiation (R_n) in Eq. [10] is calculated as (Saaltink et al., 2005):

$$R_n = (1 - A_l)R_g + \varepsilon R_g - \varepsilon\sigma T^4 \qquad [A20]$$

where R_g is the direct solar short wave radiation [E L^{-2} T^{-1}], R_a is the long wave atmospheric radiation [E L^{-2} T^{-1}], A_l is the albedo, ε is the emissivity, and σ is the Stefan–Boltzman constant. Details of the formulation can be found in Saaltink et al. (2005).

Verification and Validation of Energy and Vapor Transport

Energy and vapor transport were verified and validated by simulating a vapor transport and condensation experiment in a sandy column (Mizayaki, 1976, Fig. 14A). The columns were placed vertically in a heated chamber with constant air temperature and a relative humidity between 85 and 90%. The column tops were exposed to moist air, while the closed bottoms of the columns were maintained at room temperature in a water bath. Because of differences in vapor density, water vapor diffused from the hot and humid end of the column toward the cold and dry end, where it condensed. Subsequently, the condensed water moved upward due to the pressure head gradients.

This column experiment was previously modeled by Sakai et al. (2009) with HYDRUS-1D (Simunek et al., 2008); the same model parameters and boundary conditions were used here. The 0.1-m-long column was discretized uniformly into 100 finite volume cells. The initial volumetric water content and temperature were assumed to be uniformly distributed (i.e., θ_0 = 0.0045, Fig. 14B, and room temperature of 23.5°C, Fig. 14C). The upper boundary condition for water flow was imposed as in Sakai et al. (2009), given by the total incoming water flux assumed to be equal to the change in weight of the entire column, thus reflecting the condensation of water vapor. An impervious boundary for flow was considered at the lower boundary (see Fig. 14A), and temperatures of 36.3 and 23.5°C were imposed at the top and bottom of the column, respectively (see Fig. 14A). As in Sakai et al. (2009), the water content profiles were calculated using the soil hydraulic function parameter model by Fayer and Simmons (1995).

Experimental data (Mizayaki, 1976; Sakai et al., 2009) and simulated vertical distribution of water contents at different times (i.e., 0, 5, 10, 16, and 30 d, respectively) are shown in Fig. 14B. Temperature distribution at different times (i.e., 0.1, 0.2, 6, and 16 d, respectively) are shown in Fig. 14C. A very good agreement

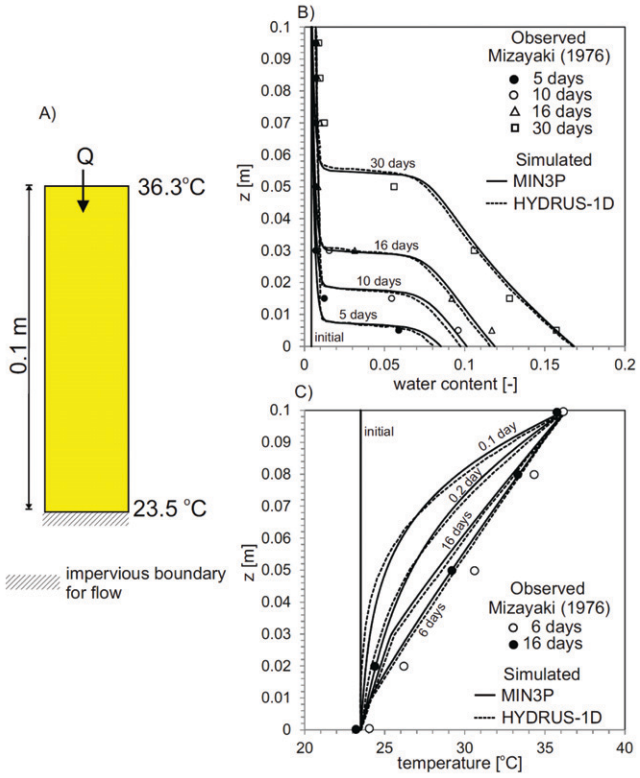

Fig. A1. Verification of energy and vapor transport: vapor condensation in a sandy column, experimental data from Mizayaki (1976). (A) Domain and boundary conditions. (B) Vertical distribution of water contents at different times. (C) Temperature distributions at different times. Results are compared with the model HYDRUS-1D (Simunek et al., 2008; Sakai et al., 2009).

with experimental data and simulated results from HYDRUS-1D was obtained by MIN3P.

Field Sampling and Quantitative Mineralogical Methods

Samples were collected at random intervals within tailings situated along the access road of Cell 2 of TSF1. Tailings were primarily sampled by coring, either as isolated core samples or on 5- by 5-m grids (after Roselle et al., 1999). Cores were taken at regular intervals of distance (0.25 and 2.50 m) and depth (10-cm-long samples centered at depths of 5, 25, 50, 75, 100, and 125 cm). Sampling did not extend to the base of the tailings deposits in most regions of TSF1 because depths greater than 1 to 4 m were inaccessible using the collection techniques available. A random number generator was used to select subsets of samples collected from cores and grids for quantitative phase analysis.

Quantitative phase analysis with the Rietveld method (Rietveld, 1969; Hill and Howard, 1987; Bish and Howard, 1988) was done on 30 samples of mine tailings from TSF1. Samples were dried in a hood under ambient laboratory conditions for at least 1 wk and were prepared for quantitative phase analysis according the method of Wilson et al. (2006). X-ray diffraction data for refinement were collected with a step size of 0.04° 2θ and counting time of 1 s step^{-1} over a range of 3 to 80° 2θ on a Siemens (Bruker AXS, Karlsruhe, Germany) D5000 θ-2θ diffractometer equipped with a VÅNTEC-1 detector in the Department of Earth and Ocean Sciences at the University of British Columbia. The long, fine-focus Co X-ray tube was operated at 35 kV and 40 mA. Mineral phases were identified with reference to the ICDD PDF-4+ database using DIFFRAC^{plus} EVA Version 10.0 (Bruker AXS, 2004a). Rietveld refinements were done using the Topas Version 3 software package (Bruker AXS, 2004b) using the fundamental parameters approach (Cheary and Coelho, 1992). The method of Wilson et al. (2006) was used to compensate for structural disorder in serpentine-group minerals during refinement.

Acknowledgments

This work was funded by the Carbon Management Canada National Centre of Excellence, the Natural Sciences and Engineering Research Council of Canada (NSERC) through the Discovery, Collaborative Research and Development, and Discovery Accelerator Supplement programs. Field sampling was supported financially in-kind by BHP Billiton and Diavik Diamond Mines. S.A. Wilson was supported by an Alexander Graham Bell Canada Graduate Scholarship from NSERC. I.M. Power was supported by a Post-Graduate Scholarship from NSERC. Mineralogical analyses and fieldwork were supported in part by a grant from the Edward H. Kraus Crystallographic Research Fund to S.A.W. from the Mineralogical Society of America.

References

Acero, P., C. Ayora, J. Carrera, M. Saaltink, and S. Olivella. 2009. Multiphase flow and reactive transport model in vadose tailings. Appl. Geochem. 24:1238–1250. doi:10.1016/j.apgeochem.2009.03.008

Ackerer, P., A. Younes, and R. Mose. 1999. Modeling variable density flow and solute transport in porous medium: 1. Numerical model and verification. Transp. Porous Media 35:345–373. doi:10.1023/A:1006564309167

Bea, S., C. Ayora, J. Carrera, M. Saaltink, and B. Dold. 2010a. Geochemical and environmental controls on the genesis of soluble efflorescent salts in coastal mine tailings deposits: A discussion based on reactive transport modeling. J. Contam. Hydrol. 111:65–82. doi:10.1016/j.jconhyd.2009.12.005

Bea, S., J. Carrera, C. Ayora, and F. Batlle. 2010b. Pitzer algortithm: Efficient implementation of Pitzer equations in geochemical and reactive transport models. Comput. Geosci. 36:526–538. doi:10.1016/j.cageo.2009.09.004

Bea, S., J. Carrera, F. Batlle, C. Ayora, and M. Saaltink. 2009. CHEPROO: A Fortran 90 object-oriented module to solve chemical processes in Earth Science models. Comput. Geosci. 35:1098–1112. doi:10.1016/j.cageo.2008.08.010

Bea, S.A., J. Carrera, J.M. Soler, C. Ayora, and M. Saaltink. 2004. Simulation of remediation alternatives for a ^{137}Cs contaminated soil. Radiochim. Acta 92:827–833. doi:10.1524/ract.92.9.827.54981

Bea, S.A., K.U. Mayer, and K.T.B. MacQuarrie. 2011. Modelling reactive transport in sedimentary rock environments—Phase II. Reactive transport modeling in a sedimentary basin affected by a glaciation/deglaciation event. Technical Rep. Nuclear Waste Management Organization, Toronto, ON, Canada.

Bish, D.L., and S.A. Howard. 1988. Quantitative phase analysis using the Rietveld method. J. Appl. Cryst. 21:86–91. doi:10.1107/S0021889887009415

Bittelli, M., F. Ventura, G. Campbell, R. Snyder, F. Gallegati, and P. Rossi Pisa. 2008. Coupling of heat, water vapor, and liquid water fluxes to compute evaporation in bare soils. J. Hydrol. 362:191–205. doi:10.1016/j.jhydrol.2008.08.014

Bruker AXS. 2004a. EVA V. 10.0: Release 2004—User's manual. Bruker AXS, Karlsruhe, Germany.

Bruker AXS. 2004b. Topas V. 3.0: General profile and structure analysis software for powder diffraction data. Bruker AXS, Karlsruhe, Germany.

Cass, A., G. Campbell, and T. Jones. 1984. Enhancement of thermal water vapor diffusion in soil. Soil Sci. Soc. Am. J. 48:25–32. doi:10.2136/sssaj1984.03615995004800010005x

Cheary, R.W., and A.A. Coelho. 1992. A fundamental parameters approach to X-ray line-profile fitting. J. Appl. Cryst. 25:109–121. doi:10.1107/S0021889891010804

Chou, L., R.M. Garrels, and R. Wollast. 1989. Comparative study of the kinetics and mechanisms of dissolution of carbonate minerals. Chem. Geol. 78:269–282. doi:10.1016/0009-2541(89)90063-6

Chung, S., and R. Horton. 1987. Soil heat and water flow with a partial surface mulch. Water Resour. Res. 23:2175–2186. doi:10.1029/WR023i012p02175

De Windt, L., F. Marsal, E. Tinseau, and D. Pellegrini. 2008. Reactive transport modeling of geochemical interactions at a concrete/argillite interface, Tournemire site (France). Phys. Chem. Earth 33(Suppl. 1):S295–S305. doi:10.1016/j.pce.2008.10.035

Diersch, H., and O. Kolditz. 2002. Variable-density flow and transport in porous media: Approaches and challenges. Adv. Water Resour. 25:899–944. doi:10.1016/S0309-1708(02)00063-5

Edlefson, N., and A. Anderson. 1943. Thermodynamics of soil mix water-wetted porous media. Water Resour. Res. 35:635–649.

Fayer, M., and C. Simmons. 1995. Modified soil water retention functions for all matric suctions. Water Resour. Res. 31:1233–1238. doi:10.1029/95WR00173

Gamazo, P., S.A. Bea, M. Saaltink, J. Carrera, and C. Ayora. 2011. Modeling the interaction between evaporation and chemical composition in a natural saline system. J. Hydrol. 401:154–164. doi:10.1016/j.jhydrol.2011.02.018

Giammar, D.E., R.G. Bruant, and C.A. Peters. 2005. Forsterite dissolution and magnesite precipitation at conditions relevant for deep saline aquifer storage and sequestration of carbon dioxide. Chem. Geol. 217:257–276. doi:10.1016/j.chemgeo.2004.12.013

Gran, M., J. Carrera, S. Olivella, and M. Saaltink. 2011. Modeling evaporation processes in a saline soil from saturation to oven dry conditions. Hydrol. Earth Syst. Sci. Discuss. 8:529–554. doi:10.5194/hessd-8-529-2011

Harvie, C.E., N. Moller, and J.H. Weare. 1984. The prediction of mineral solubilities in natural waters: The Na–K–Mg–Ca–H–Cl–SO_4–OH–HCO_3–CO_3–CO_2–H_2O system to high ionic strengths at 25°C. Geochim. Cosmochim. Acta 48:723–751. doi:10.1016/0016-7037(84)90098-X

Henderson, T., K. Mayer, B. Parker, and T. Al. 2009. Three-dimensional density-dependent flow and multicomponent reactive transport modeling of chlorinated solvent oxidation by potassium permanganate. J. Contam. Hydrol. 106:195–211. doi:10.1016/j.jconhyd.2009.02.009

Hill, R.J., and C.J. Howard. 1987. Quantitative phase analysis from neutron powder diffraction data using the Rietveld method. J. Appl. Cryst. 20:467–474. doi:10.1107/S0021889887086199

Hostetler, P.B., R.G. Coleman, F.A. Mumpton, and B.W. Evans. 1966. Brucite in alpine serpentinites. Am. Mineral. 51:75–98.

IPCC. 2005. IPCC Special Report on Carbon Dioxide Capture and Storage. B. Metzet al. (ed.) Cambridge Univ. Press, Cambridge, UK.

IPCC. 2007. Climate Change 2007: The physical basis. Contribution of Working Group I to the Fourth Assessment Report of the Intergovernmental Panel on Climate Change. S. Solomon et al. (ed.) Cambridge Univ. Press, Cambridge, UK.

Kolditz, O., R. Ratke, H.J.G. Diersch, and W. Zielke. 1998. Coupled groundwater flow and transport: 1. Verification of variable density flow and transport models. Adv. Water Resour. 21:27–46. doi:10.1016/S0309-1708(96)00034-6

Königsberger, E., L.C. Königsberger, and H. Gamsjäger. 1999. Low-temperature thermodynamic model for the system Na_2CO_3–$MgCO_3$–$CaCO_3$–H_2O. Geochim. Cosmochim. Acta 63:3105–3119. doi:10.1016/S0016-7037(99)00238-0

Krumgalz, B.S., A. Hecht, A. Starinsky, and A. Katz. 2000. Thermodynamic constraints on Dead Sea evaporation: Can the Dead Sea dry up? Chem. Geol. 165:1–11. doi:10.1016/S0009-2541(99)00156-4

Lackner, K.S. 2003. A guide to CO_2 sequestration. Science 300:1677–1678. doi:10.1126/science.1079033

Lefebvre, R., D. Hockley, J. Smolensky, and P. Gelinas. 2001a. Multiphase transfer processes in waste rock piles producing acid mine drainage I: Conceptual model and system characterization. J. Contam. Hydrol. 52:137–164. doi:10.1016/S0169-7722(01)00156-5

Lefebvre, R., D. Hockley, J. Smolensky, and P. Gelinas. 2001b. Multiphase transfer processes in waste rock piles producing acid mine drainage II: Applications of numerical simulation. J. Contam. Hydrol. 52:165–186. doi:10.1016/S0169-7722(01)00157-7

Lever, D.A., and C. Jackson. 1985. On the equations for the flow of concentrated salt solution through a porous medium. Technical report, U.K. DOE Rep. DOE/RW/85.100.

Lichtner, P., and Q. Kang. 2007. Upscaling pore-scale reactive transport equations using a multi-scale continuum formulation. Water Resour. Res. 43:W12S15. doi:10.1029/2006WR005664

Massmann, J., and D. Farrier. 1992. Effects of atmospheric pressures on gas transport in the vadose zone. Water Resour. Res. 28:777–791. doi:10.1029/91WR02766

Mayer, K.U., E.O. Frind, and D.W. Blowes. 2002. Multicomponent reactive transport modeling in variably saturated porous media using a generalized formulation for kinetically controlled reactions. Water Resour. Res. 38:1174. doi:10.1029/2001WR000862.

Millington, R.J. 1959. Gas diffusion in porous media. Science 130:100–102. doi:10.1126/science.130.3367.100-a

Mizayaki, T. 1976. Condensation and movement of water vapor in sand under temperature gradient. (In Japanese.) Trans. Jpn. Soc. Irrig. Drain. Reclam. Eng. 61:1–8.

Molins, S., and K. Mayer. 2007. Coupling between geochemical reactions and multicomponent gas and solute transport in unsaturated media: A reactive transport modeling study. Water Resour. Res. 43:W05435. doi:10.1029/2006WR005206

Molins, S., K. Mayer, C. Scheutz, and P. Kjeldsen. 2008. Transport and reaction processes affecting the attenuation of landfill gas in cover soils. J. Environ. Qual. 37:459–468. doi:10.2134/jeq2007.0250

Monnin, C. 1994. Density calculation and concentration scale conversions for natural waters. Comput. Geosci. 20:1435–1445. doi:10.1016/0098-3004(94)90103-1

Noborio, K., K. McInnes, and J. Heilman. 1996. Two-dimensional model for water, heat, and solute transport in furrow-irrigated soil. I. Theory. Soil Sci. Soc. Am. J. 60:1001–1009. doi:10.2136/sssaj1996.03615995006000040007x

Olivella, S., J. Carrera, A. Gens, and E.E. Alonso. 1994. Nonisothermal multiphase flow of brine and gas through saline media. Transp. Porous Media 15:271–293. doi:10.1007/BF00613282

Palandri, J., and Y. Kharaka. 2004. A compilation of rate parameters of water-mineral interaction kinetics for application to geochemical modeling. Technical report. USGS Open-file Rep. 2004-1068.

Philip, J., and D. De Vries. 1957. Moisture movement in porous materials under temperature gradient. Trans. Am. Geophys. Union 38:222–232.

Pokrovsky, O., and J. Schott. 1999. Processes at the magnesium-bearing carbonates/solution interface. II. Kinetics and mechanism of magnesite dissolution. Geochim. Cosmochim. Acta 63:881–897. doi:10.1016/S0016-7037(99)00013-7

Pokrovsky, O., and J. Schott. 2004. Experimental study of brucite dissolution and precipitation in aqueous solutions: Surface speciation and chemical affinity control. Geochim. Cosmochim. Acta 68:31–45. doi:10.1016/S0016-7037(03)00238-2

Pokrovsky, O., S.V. Golubev, and J. Schott. 2005. Dissolution kinetics of calcite, dolomite and magnesite at 25°C and 0 to 50 atm pCO_2. Chem. Geol. 217:239–255. doi:10.1016/j.chemgeo.2004.12.012

Power, I.M., S.A. Wilson, J.M. Thom, G.M. Dipple, J.E. Gabites, and G. Southam. 2009. The hydromagnesite playas of Atlin, British Columbia, Canada: A biogeochemical model for CO_2 sequestration. Chem. Geol. 260:286–300. doi:10.1016/j.chemgeo.2009.01.012

Rietveld, H. 1969. A profile refinement method for nuclear and magnetic structures. J. Appl. Cryst. 2:65–71. doi:10.1107/S0021889869006558

Roselle, G.T., L.P. Baumgartner, and J.W. Valley. 1999. Stable isotope evidence of heterogeneous fluid infiltration at the Ubehebe Peak contact aureole, Death Valley National Park, California. Am. J. Sci. 299:93–138.

Saaltink, M.W., C. Ayora, and S. Olivella. 2005. User's guide for RetrasoCodeBright (RCB). Department of Geotechnical Engineering and Geo-Sciences, Technical Univ. of Catalonia (UPC), Barcelona, Spain.

Saito, H., J. Simunek, and B. Mohanty. 2006. Numerical analyses of coupled water, vapor and heat transport in the vadose zone. Vadose Zone J. 5:784–800. doi:10.2136/vzj2006.0007

Sakai, M., N. Toride, and J. Simunek. 2009. Water and vapor movement with condensation and evaporation in a sandy column. Soil Sci. Soc. Am. J. 73:707–717. doi:10.2136/sssaj2008.0094

Sayles, F.L., and W.S. Fyfe. 1973. Crystallization of magnesite from aqueous-solution. Geochim. Cosmochim. Acta 37:87–99. doi:10.1016/0016-7037(73)90246-9

Seifritz, W. 1990. CO_2 disposal by means of silicates. Nature 345:486. doi:10.1038/345486b0

Simunek, J., M. Sejna, H. Saito, M. Sakai, and M. van Genuchten. 2008. The HYDRUS-1D software package for simulating the movement of water, heat, and multiple solutes in variably saturated media. version 4.0. Hydrus Softw. Ser. 3. Tech. rep. Dep. of Environmental Science, Univ. of California, Riverside.

Simunek, J., M. Sejna, H. Saito, M. Sakai, and M. van Genuchten. 2009. The HYDRUS-1D software package for simulating the one dimensional movement of water, heat, and multiple solutes in variably-saturated media. version 4.08. Hydrus Softw. Ser. 3. Tech. rep. Dep. of Environmental Science, Univ. of California, Riverside.

Sipilä, J., S. Teir, and R. Zevenhoven. 2008. Carbon dioxide sequestration by mineral carbonation: Literature review update 2005–2007. Åbo Akademi Rep. VT 2008-1.

Stolberg, D.J. 2005. Rehabilitation studies on tailings storage facilities in an arid hypersaline region. Ph.D. diss. Div. of Civil Engineering, School of Engineering, Univ. of Queensland, Brisbane, Australia.

Thom, J., and G.M. Dipple. 2005. Accelerated cation release during non-steady state dissolution of Mg-silicates: Implications for mine tailings and sequestration of CO_2. Paper 29. *In* Fourth Annual Conference on Carbon Capture and Sequestration, 2–5 May 2005, Alexandria, VA.

Voss, C. 1984. A Finite-element simulation model for saturated-unsaturated fluid-density-dependent ground-water flow with energy transport or chemically-reactive single-species solute transport. USGS Water Resour. Invest. Rep. 84-4369.

Voss, C., and A. Provost. 2008. SUTRA—A model for saturated-unsaturated variable-density ground-water flow with solute or energy transport (Version 2.1). USGS Water Resour. Invest. Rep. 02-4231.

White, A.F., and M.L. Peterson. 1990. Role of reactive-surface-area characterization in geochemical kinetic models. Chapter 35, p. 461–475. *In* D.C. Melchior and R.L. Bassett (ed.) Chemical modeling of aqueous systems II. American Chemical Society, Washington, DC.

Wilson, S. 2009. Mineral traps for greenhouse gases in mine tailings: A protocol for verifying and quantifying CO_2 sequestration in ultramafic mines. Ph.D. diss. The Faculty of Graduate Studies (Geological Sciences). The University of British Columbia.

Wilson, S., G. Dipple, I. Power, J. Thom, R. Anderson, M. Raudsepp, J. Gabites, and G. Southam. 2009. Carbon dioxide fixation within mine wastes of ultramafic-hosted ore deposits: Examples from the Clinton Creek and Cassiar chrysotile deposits, Canada. Econ. Geol. 104:95–112. doi:10.2113/gsecongeo.104.1.95

Wilson, S., M. Raudsepp, and G. Dipple. 2006. Verifying and quantifying carbon fixation in minerals from serpentine-rich mine tailings using the Rietveld method with X-ray powder diffraction data. Am. Mineral. 91:1331–1341. doi:10.2138/am.2006.2058

Wösten, J., and M. van Genuchten. 1988. Using texture and other soil properties to predict the unsaturated soil hydraulic functions. Soil Sci. Soc. Am. J. 52:1762–1770. doi:10.2136/sssaj1988.03615995005200060045x

Xiong, Y., and A.S. Lord. 2008. Experimental investigations of the reaction path in the MgO-CO_2–H_2O system in solutions with various ionic strengths, and their applications to nuclear waste isolation. Appl. Geochem. 23:1634–1659. doi:10.1016/j.apgeochem.2007.12.035

Xu, T., S. White, K. Pruess, and G. Brimhall. 2000. Modeling of pyrite oxidation in saturated and unsaturated subsurface flow systems. Transp. Porous Media 39:25–56. doi:10.1023/A:1006518725360